2010-01-15

Simulating the FTICR-MS Signal of a Decaying Beryllium-7 Ion Plasma in a 2D Electrostatic PIC Code

Michael Takeshi Nakata
Brigham Young University - Provo

Simulating the FTICR-MS Signal of a Decaying Beryllium-7

Ion Plasma in a 2D Electrostatic PIC Code

Michael Takeshi Nakata

A dissertation submitted to the faculty of
Brigham Young University
in partial fulfillment of the requirements for the degree of

Doctor of Philosophy

Grant W. Hart, Chair
Bryan G. Peterson
Ross L. Spencer
David V. Dearden
Eric W. Hirschmann

Department of Physics and Astronomy

Brigham Young University

April 2010

ABSTRACT

Simulating the FTICR-MS Signal of a Decaying Beryllium-7

Ion Plasma in a 2D Electrostatic PIC Code

Michael Takeshi Nakata

Department of Physics and Astronomy

Doctor of Philosophy

Beryllium-7 (Be-7) only decays by electron capture into lithium-7 (Li-7) with a half life of 53 days. We study the effect of ionization on this decay rate. We do so by trapping a Be-7 ion plasma in a cylindrical Malmberg-Penning trap and measuring Be-7 and Li-7 concentrations as functions of time by using Fourier transform ion cyclotron resonance mass spectrometry (FTICR-MS).

We have simulated these signals in a 2-dimensional electrostatic particle-in-cell (PIC) code. The two spectrum peaks merge at high ion densities whereas at low ion densities they can be resolved. The merged peak shifts linearly according to the relative abundances of these species.

We have also simulated singly-ionized beryllium-7 hydride (BeH+) and Li-7 ion plasmas at high densities. These two separate peaks shift according to their relative abundances. We describe an analytical model that explains how these peaks shift.

ACKNOWLEDGMENTS

I would like to first acknowledge my Lord God's hand throughout this project, dissertation, and endeavor. His hand has been there for me each day at each crossroad. I am so grateful for His love, support, care, and personal interest in me and my family.

Thanks to my wife Maria for joining me in this endeavor and believing in me. Thanks to our two sons Nephi and Kouji who have brought joy and balance to my life. Thanks to my extended family for their prayers and support of our family.

Thanks to Dr. Grant Hart for his optimism, guidance, and advice on this project. Thanks to Dr. Bryan Peterson for maintaining "maxwell2" computer up and running, getting me experimental parameters and data, and making our references available online. Thanks to Dr. Ross Spencer for previous code, assistance in coding a PIC code, and theoretical insight. Thanks to Dr. Eric Hirshmann for a fresh pair of eyes over my dissertation work. Thanks to Dr. David Dearden for his enthusiasm and experimental insights to this field of FTICR-MS.

Thanks to the Department of Physics and Astronomy for the opportunity to be a teaching and research assistant. Thanks to the College of Physical and Mathematical Science and Copley funding for financial support. Thanks to Fulton Supercomputing Lab and its staff for support and computer resources.

CONTENTS

LIST OF FIGURES

1.1 ^{7}BE, AN INTERESTING SCIENTIFIC TOOL

Beryllium-7 (^{7}Be) is the lightest element to decay solely by electron capture to Lithium-7 (^{7}Li). It does so with a half life of about 53 days.[1,2] It usually decays as follows:

$$^7Be + e^- \rightarrow \, ^7Li + \nu_e + 861.8 \text{ keV} \qquad (89.6\%)$$

$$^7Be + e^- \rightarrow \, ^7Li^* + \nu_e + 384.2 \text{ keV} \qquad (10.4\%)$$

$$^7Li^* \rightarrow \, ^7Li + \gamma + 477.6 \text{ keV}$$
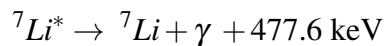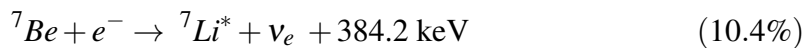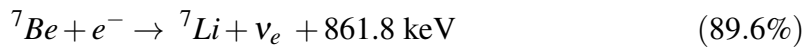
90% of the time, it decays directly to lithium-7 (^{7}Li) with most of the decay energy of 861.8 keV being carried by the electron neutrino (ν_e). 10% of the time, it decays to an excited ^{7}Li* state with a 384.2 keV electron neutrino. This subsequently decays to the ground state and releases a photon (γ) with 477.6 keV energy. This was first observed by Roberts, Heydenburg, and Locher[3] in lithium and boron targets.

One interesting aspect of ^{7}Be is how it has been used as a scientific instrument to probe our universe. Its reactions were used to indirectly confirm the existence of neutrinos.[4] Its discovery[5] in our atmosphere from cosmic-ray spallation of nitrogen and oxygen has led to its becoming a tracer for atmospheric transport and other geophysical processes. Its decay reaction, found in the solar proton-proton fusion cycle, was first used to probe the sun's interior to better understand this cycle.[6]

Environment	$T_{1/2}$ (days)	Reference
endohedral C_{60}	52.68 ± 0.05	Ohtsuki *et. al*[7]
Be(OH)$_2$ at 442 kbar	52.884 ± 0.022	Huh[8]
BeO	54.226 ± 0.006	Liu and Huh[9]

TABLE 1.1 Half-Life of ^{7}Be in various environments

Another interesting aspect of ^{7}Be is how its decay rate is affected by the electron density around the nucleus. Segre[10] was among the first to propose studying this effect on ^{7}Be's decay rate. Since then, many researchers have observed a 1 to 2% change in the half life of ^{7}Be when it is placed in different electronic environments. Table 1.1 lists some of these measurements under various conditions. Since oxygen pulls the electrons away from the ^{7}Be nucleus site, its decay rate decreases in BeO. For both the ^{7}Be in a buckyball C_{60} and under 442 kbar of pressure in Be(OH)$_2$, the electrons move toward the nucleus thereby increasing the decay rate.

To our knowledge no one has studied the decay rate when ionized, which would be its most natural state in our upper atmosphere and sun. We desire to study this effect on the half life of ^{7}Be. Hutchison[11] in our plasma group used both Hartree-Fock self-consistent field and Density Functional Theory methods to calculate the relative changes in the decay constants for ^{7}Be, ^{7}Be$^+$, and ^{7}Be^{++} and found that the decay rate for singly-ionized ^{7}Be would increase compared to its accepted values.

1.2 OUR ^{7}BE EXPERIMENT

To study the half life of ionized ^{7}Be, we require an experimental apparatus that can confine 10^9 ionized ^{7}Be ions for a period on the order of the half life. Our group has devised such a system as shown in the Figure 1.1.
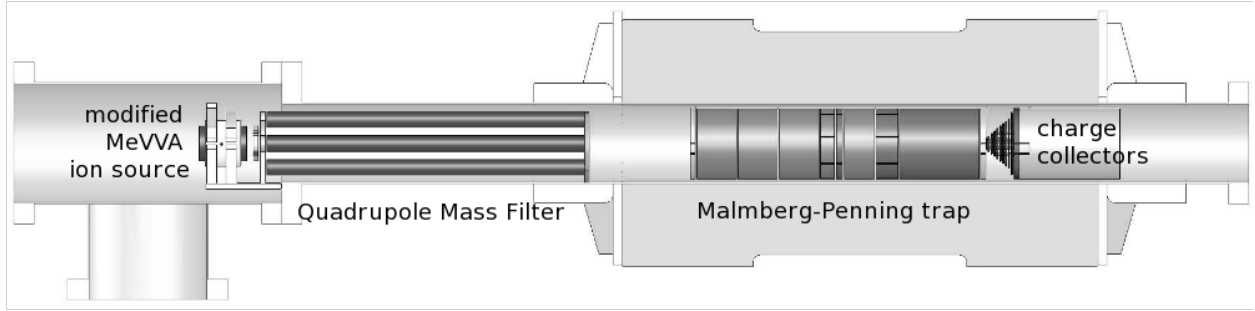
FIG. 1.1 Overview schematic of our ^{7}Be experiment. The B$_4$C sample is inserted into the modified MeVVA ion source. The Quadrupole Mass Filter (QMF) filters the mass contaminants. The Malmberg-Penning traps our ^{7}Be ions axially by electrostatic end electrodes. The outer solenoid (which is part of the trap) confines the ions radially by producing an axial magnetic field of a strength of about 0.43 T. The whole experiment is evacuated between 10^{-9} to 5×10^{-10} torr.

The process begins by locally creating ^{7}Be by bombarding an isotopically enriched boron carbide (B$_4$C) sample with a proton beam with an average energy of 400 keV in a Van de Graaff accelerator. The nuclear reaction that occurs in the B$_4$C is as follows:

$$^{10}B + p^+ \rightarrow {}^7Be + {}^4He \tag{1.1}$$

This creates ^{7}Be in the B$_4$C sample and ejects alpha particles (^{4}He).

The sample is moved from the accelerator and inserted into a Metal Vapor Vacuum Arc (MeVVA) ion source.[12] We then eject the ^{7}Be ions from the sample by arcing across the surface with high voltage in this ion source. This not only releases ^{7}Be from the B$_4$C sample, but also other contaminants like B and C ions.

We filter these contaminants from the ^{7}Be ions by applying alternating and DC voltages on four poles in a quadrupole mass filter (QMF).[13] The QMF also channels them into our trap's high magnetic field, which tends to deflect particles away from the trap by mirroring them if they have too much transverse velocity.

After the ions enter the trap region they are confined radially by applying an axial magnetic
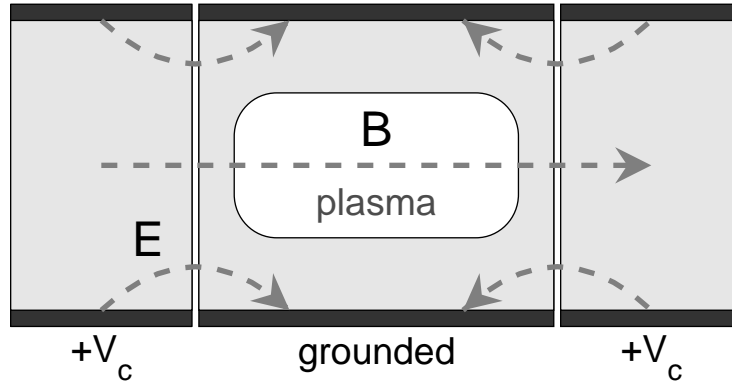
FIG. 1.2 A nonneutral plasma is confined radially by an axial magnetic field. It is confined in the axial direction by electrostatic potential V_c on the two end electrodes of a Malmberg-Penning trap. The trap region remains grounded.

field. They are confined in the axial direction by electrostatic potentials on end electrodes in a Malmberg-Penning trap.[14] Figure 1.2 shows how these ions are confined. In our trap, we can repeat the firing of the ion source and channeling through the QMF sequence as many times as we need to collect 10^9 ^{7}Be ions.

We plan to hold this ^{7}Be ion plasma for its half life by using a rotating wall technique which was pioneered in these machines.[15] Normally, small static field errors and background neutral gas exert a drag on the rotating nonneutral plasma which causes it to slowly expand and be lost to the wall. The rotating wall technique works by applying a "rotating wall" electric field on the plasma at a rate faster than its natural rotation frequency. This frequency is the $\mathbf{E} \times \mathbf{B}$ rotation frequency of the plasma at $r = 0$. As a result, the nonneutral plasma spins up and compresses into a steady-state equilibrium.

To determine the decay rate of ^{7}Be ions, we can either detect the 477.6 keV gamma emitted in 10.4% of the decays or observe the increase of ^{7}Li ions in the plasma. The cylindrical geometry of our trap makes it difficult to detect the isotropic gamma emissions, so we will use a sectored ring on our trap to detect the ^{7}Li ions in the plasma using a Fourier transform ion cyclotron resonance

mass spectrometry (FTICR-MS) technique.[16] Finally, we will use a set of charge collecting disks connected to an integrator circuit[17] to destructively measure the radial profile of our plasma when it is dumped out the end of the trap.

THEORY AND PREVIOUS WORK

2.1 FTICR-MS

Fourier transform ion cyclotron resonance mass spectrometry (FTICR-MS)[18,19] is based on the fact that charged particles in a uniform magnetic field exhibit a circular motion known as cyclotron motion. The frequency of these orbits depends on the charge-to-mass ratio of the ions q/m and on the magnetic field B.

$$f_c = \frac{1}{2\pi}\frac{q}{m}B \tag{2.1}$$

If the uniform magnetic field strength is known and the charge is the same for all the confined ions in the trap, we can determine the composition and abundance of the ions by observing which cyclotron frequencies are present and the strength of the signal at each frequency.

In our trap we use a 4-segmented cylindrical electrode to excite and detect the cyclotron motion. Initially, the cyclotron signal from the confined ions cannot be detected because the thermal energy distribution and their random phases with each other make the signal too small to see. To detect a measurable signal, we apply a dipolar oscillating voltage signal on two opposing sectors near the ions' cyclotron frequencies. This creates an approximately uniform electric field which oscillates at the cyclotron frequency and therefore accelerates the ions outward as shown in Fig. 2.1. This makes the orbits larger and re-phases the orbits so all the ions are in phase with each other. This much larger induced signal is then detected on two other opposing sectors. This signal is then fast Fourier transformed (FFT) to obtain a frequency spectrum which characterizes the confined ions in

the trap. Provided we excite within the range of frequencies that cover the expected ion masses, it becomes possible to determine the relative abundances of the ions by the amplitude of the signals at the associated cyclotron frequencies.
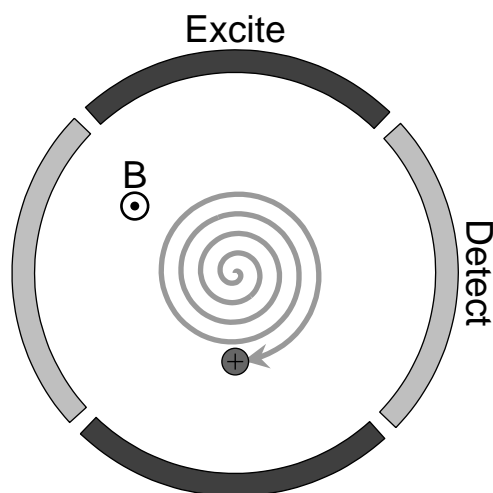
FIG. 2.1 FTICR-MS consists of using the dark grey sectors to excite the cyclotron motion of the confined ions. As energy is added to these ions, they spiral out as shown by the light grey path. After excitation, the light grey sectors detect the induced signal from the excited ions. Finally, this induced signal is fast Fourier transformed to obtain the frequency spectrum which characterizes these confined ions in the trap.

One of the fundamental limitations of FTICR-MS is the presence of external and self electric fields. These fields cause an $\mathbf{E} \times \mathbf{B}$ drift on the confined ions. This drift causes the entire charge column to rotate. This rotation causes the cyclotron frequency to be downshifted by a certain rotation frequency associated with the drift. For normal FTICR-MS systems at low densities, this is primarily the magnetron frequency which comes from the radially confining electric fields. Nevertheless, there is also a small contribution from the image charges on the wall which increases as the number of ions increases. For nonneutral plasmas like ours, this is the diocotron frequency, which results in the rotation of an offset plasma around the symmetry axis of the confining walls.

It is due to the radial electric fields from the image charges on the wall.

The measured ion cyclotron resonance frequency f_{icr} is always the cyclotron frequency f_c downshifted by the rotation frequency f_d associated with the $\mathbf{E} \times \mathbf{B}$ drift where the $\mathbf{E}$ is the trap and image electric field.

$$f_{icr} = f_c - f_d \tag{2.2}$$

2.2 PREVIOUS WORK: PLASMA LIMITATIONS

Another limitation of FTICR-MS which particularly affects our system is that our ion cloud is a nonneutral plasma. A nonneutral plasma is defined as a gas of charged particles that exhibits collective behavior. This collective behavior comes from the long-range Coulomb interaction of charged particles. There are two main conditions that a charge cloud must satisfy to be a plasma.

$$\lambda_D \ll L \tag{2.3}$$

$$\omega_p > \nu_c \tag{2.4}$$

Condition one is that its Debye length, λ_D, is shorter than the physical dimensions, L, of the plasma. Condition two is that the typical plasma oscillation frequency, ω_p, is greater than the mean collision rate, ν_c. In our case, the Debye length is 377 μm which is much less than the radius of our plasma which is 2 cm. Our plasma frequency is 251 kHz, which is much greater than ion-ion collision frequency of 417 Hz.

As the number of ions increases in the cloud, not only is there an image charge related frequency shift, but there are Coulomb interactions between the ions, which then behave collectively. This electrostatic coupling causes clouds of similar mass species to phase lock.[20,21] It also causes other frequency shifts that are not well understood because of the collective behavior of a plasma.

Some of the initial work to understand this Coulomb interaction was done by Jeffries *et. al*[22] for a weak space charge effect. Later, Gorshkov, Marshall and Nikolaev[23] considered two species with a line charge model, with both line charges orbiting at the same radius. However, none of these works can fully explain an ion cloud which is a nonneutral plasma.

In two FTICR-MS experiments, Huang *et al.*[20] and Naito and Inoue[21] observed that the spectral peaks for similar mass species coalesced at high densities. Peurrung and Kouzes[24] generalized this as part of the phenomena exhibited by coupled gyrators. Naito and Inoue[21,25] modeled this phenomenon with two singly-charged particles confined in a plane perpendicular to a uniform magnetic field. They calculated that one of the mode frequencies of this four-degrees-of-freedom system is at the molecular-number weighted average of the two individual cyclotron frequencies. They speculate that this frequency is the frequency of the coalesced peak.

Using a two-cylindrical ion cloud numerical simulation, Mitchell and Smith[26] observed that the frequency after phase locking was almost, but not quite, the weighted average of their unperturbed cyclotron frequencies. In a subsequent paper[27], they observed that there was a relative ion abundance dependence on the single collective cyclotron frequency of cylindrical ion clouds. In this paper, they study extensively the various parameters which effect the phase locking of ion clouds. Mitchell[28] further simulated this phenomenon in a 3D PIC code. He noticed that the frequency at phase locking for two equal amounts of two species was an average of the two shifted unperturbed cyclotron frequencies. This shift was due to the image charge interaction between the phase-locked ion cloud and the conducting wall. He used the Gorshkov *et. al*[23] calculation of the image charge frequency shift for a line charge inside a grounded cylindrical trap. This result Mitchell thought was fortuitous because his simulation was in a cubic trap and not in an infinitely long cylindrical trap.

Recently, Boldin and Nikolaev[29] have revisited the theory of peak coalescence in FTICR-MS. They describe the motion of the ion clouds in terms of their averaged drift motion in a crossed

magnetic and electric fields. They assume ion clouds of constant size and their motion is studied in two dimensions. They use a first-order approximation of the equations of motion in relation to dm/m, where dm is the mass difference and m is the mass of a single ions. They focused their study on the onset of coalescence in an arbitrary interaction potential. Using their condition of the onset of coalescence for uniformly charged spheres, our simulation (which has a different geometry) agrees with their results within reasonable approximations.

In a pure electron plasma, Gould and Lapointe[30] observed that the $m = 1$ cyclotron mode had a frequency equal to the cyclotron frequency downshifted by the diocotron frequency. In a nonneutral Mg^+ ion plasma, Sarid, Anderegg, and Driscoll[31] observed a shift in these cyclotron modes. They could explain these shifts for the major species with a multispecies cold plasma theory, but not for the minor species. They used Davidson's[32] multispecies cold plasma theory to explain their frequency shifts for the major species.

2.3 DAVIDSON'S COLD MULTISPECIES PLASMA THEORY

Davidson[32] derived an electrostatic dispersion relation for an infinitely long, constant density, nonrelativistic, multispecies nonneutral plasma column using a macroscopic cold fluid description. This plasma column with a radius R_p is confined inside a cylindrical conductor of radius R_w. The macroscopic cold fluid description consists of a linearized steady-state continuity equation, the force balance equation, and Maxwell's equations. The perturbed solutions for density, velocity, electric and magnetic fields were all Fourier decomposed in the following way:

$$\delta \psi(r,\theta,z,t) = \sum_{m=-\infty}^{\infty} \sum_{k_z=-\infty}^{\infty} \delta \psi^m(r,k_z)\exp[i(m\theta + k_z z - \omega t)] \qquad (2.5)$$

where $\delta\psi$ is any of the perturbed quantities. We choose to restrict our attention to purely azimuthal modes, so we set $k_z = 0$. So, we are left with any *m* order angular solutions. The electrostatic dispersion relation for a cold uniform density multicomponent nonneutral plasma column is:

$$0 = 1 - \sum_j \frac{\omega_{pj}^2 [1 - (R_p/R_w)^{2m}]}{2(\omega - m\omega_{rj})[(\omega - m\omega_{rj}) + (-\omega_{cj} + 2\omega_{rj})]}. \tag{2.6}$$

In this equation *m* is the angular mode number. The sum in this dispersion relation is over the species *j* of the plasma with the angular frequencies are defined as follows:

$$\omega_{cj} = \frac{eB}{m_j}, \qquad \omega_{pj}^2 = f_j\, w_{pj}^2 = f_j \frac{e^2 n_0}{m_j \varepsilon_0}, \qquad \omega_{rj} = \omega_{cj} \left[1 - \left(1 - 2\, \frac{w_{pj}^2}{\omega_{cj}^2} \right)^{1/2} \right].$$

The first angular frequency, ω_{cj} is the cyclotron oscillation. The second angular frequency, ω_{pj}, is the plasma oscillation. The m_j in these angular frequencies are the mass of species *j*. Note that we have redefined Davidson's plasma angular frequency ω_{pj} to w_{pj} where $f_j = n_j/n_0$ is the fraction of the number density and $n_0 = \sum_k n_k$ is the total density of the plasma column. The third angular frequency, ω_{rj} is related to the slow rotation of the plasma column. We have taken the sign convention to be positive for all of these angular frequencies.

This theory predicted the plasma cyclotron peak frequency shifts which were observed by Sarid *et. al*[31] for their major species. They also extended this theory to include the radial density profile dependence on these frequency shifts. However, they could not explain the shifts from the minor species.

2.4 TWO CHARGED RODS IN A GROUNDED CYLINDER MODEL

To better understand the spectral peak shifts with abundances of $^7\text{BeH}^+$ and $^7\text{Li}^+$ plasma at high density, Ross L. Spencer developed an electrostatic analytical model. The model simply consists of two infinitely long charged rods of radius R_p that are nearly centered in a grounded infinitely long cylinder of radius R_w. This model includes the radial extent of the charge column and the collective behavior of a nonneutral plasma which Gorshkov, Marshall and Nikolaev's simple line charge model[23] does not take into account.

To simplify our equations of motion, we define the total number of particles $n_0 = n_1 + n_2$ as the sum of the number of each species and the fraction of species 1, $f = n_1/n_0$, to be the ratio of the number of species 1 to the total number of particles. We also define the following angular velocities:

$$\omega_{c_1} = \frac{eB}{m_1}, \qquad \omega_{p_1}^2 = \frac{e^2 n_0}{\varepsilon_0 m_1}, \qquad \omega_{c_2} = \frac{eB}{m_2}, \qquad \omega_{p_2}^2 = \frac{e^2 n_0}{\varepsilon_0 m_2}$$

related to the cyclotron and plasma oscillation of each charged rod. The equations of motion for each charged rod are:

$$\begin{aligned}
\ddot{\mathbf{r}}_1 &= \omega_{c_1}(\dot{\mathbf{r}}_1 \times \hat{z}) &+ \frac{(1-f)}{2}\omega_{p_1}^2(\mathbf{r}_1 - \mathbf{r}_2) &+ \frac{\omega_{p_1}^2}{2}\frac{R_p^2}{R_w^2}[f\mathbf{r}_1 + (1-f)\mathbf{r}_2] \\
\ddot{\mathbf{r}}_2 &= \omega_{c_2}(\dot{\mathbf{r}}_2 \times \hat{z}) &+ \frac{f}{2}\omega_{p_2}^2(\mathbf{r}_2 - \mathbf{r}_1) &+ \frac{\omega_{p_2}^2}{2}\frac{R_p^2}{R_w^2}[f\mathbf{r}_1 + (1-f)\mathbf{r}_2].
\end{aligned} \tag{2.7}$$

The first term in this set of equations represents the magnetic force on the respective rods. The second term is the electric coupling between the two rods. For rod 1 it is the electric force from rod 2 on rod 1. The third term represents the effect of the image charge on the grounded cylindrical wall from each rod. The $\mathbf{r}_1$ term is the image charge for rod 1 while the the $\mathbf{r}_2$ term is the image

charge for rod 2.

If we assume sinusoidal time dependence $e^{-i\omega t}$, this set of equations yields a dispersion relation of 4th order in ω^2. The four roots are: (1) the diocotron mode, (2) the rotation of each rod around the other, which I name the binary mode, roots (3) and (4) are the cyclotron oscillations near the cyclotron frequency of each individual mass, but shifted by the electrostatic fields. These cyclotron oscillations vary with the fractions of the species just as our spectral peak frequency does in our simulation. I refer you to Fig. 4.9 for the agreement between the simulation and the model.

This analysis also agrees with Davidson's cold multispecies plasma dispersion relation which predicts the same four modes, but this model gives a better physical picture of what is going on in our experiment. We learn about four different physical oscillation modes which are present in Davidson's theory but not as transparent. However Davidson's theory does extend this analysis to understand the frequency shifts for two different mass species to higher *m* angular modes and to more species than two.

Using Davidson and this analytical model, we can identify the different modes of oscillation in our simulated spectrum for equal amounts of $^7BeH^+$ and $^7Li^+$ at a central density of 10^{13} m^{-3}. Figure 2.2 illustrates the two different types of oscillation modes. There are slow modes and fast modes. We are only sensitive to the odd harmonics of *m* because of our detection symmetry. In the slow modes subplot we see the binary mode. We normally would not be sensitive to the binary mode with the detection geometry, but there is a nonlinear coupling to the diocotron mode which makes it visible with a small amplitude. In the fast modes subplot, we identify each peak by its species cyclotron oscillation frequency downshifted by the diocotron frequency. These peaks change with the relative abundances of the confined species.
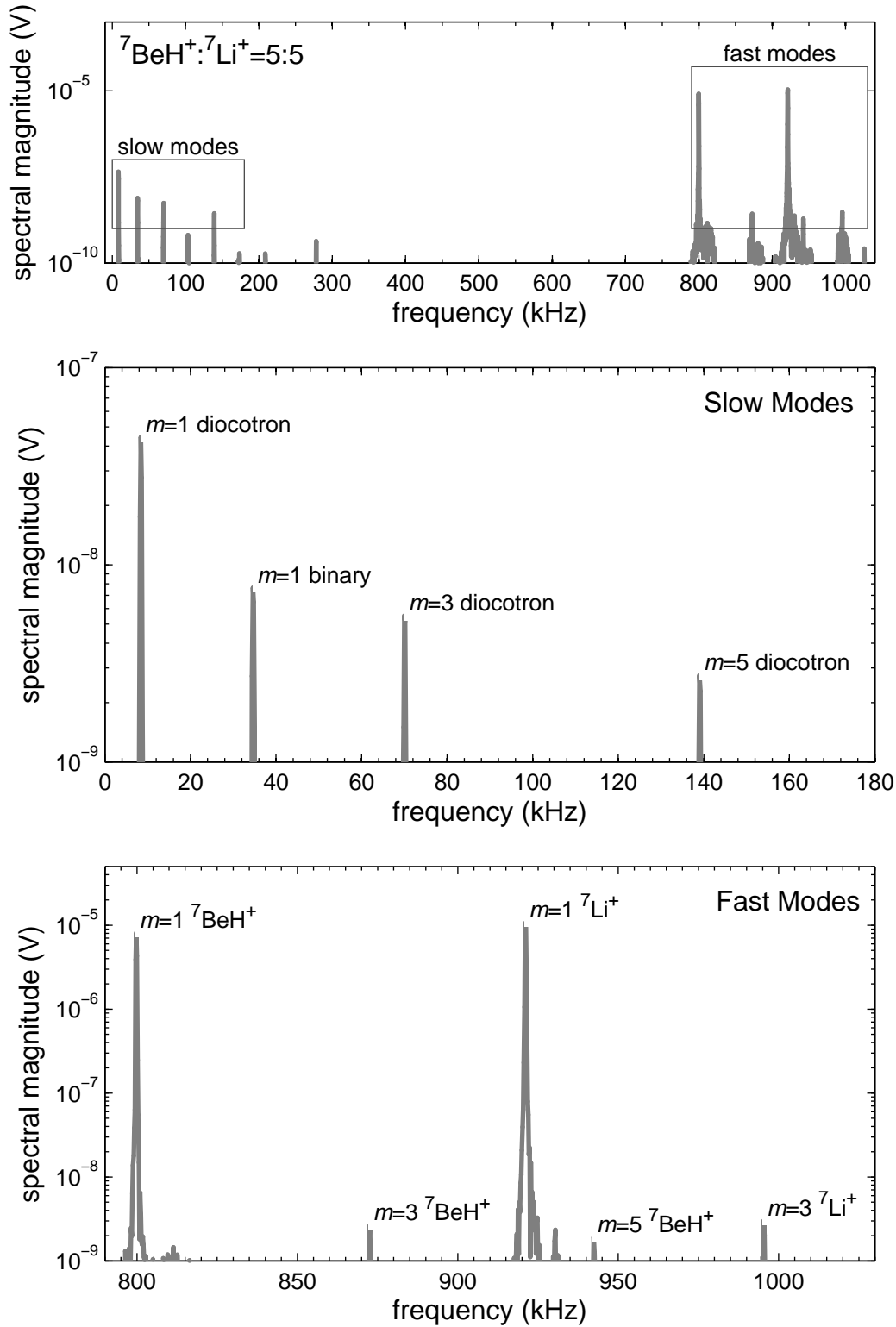
FIG. 2.2 Overall spectrum for equal amounts $^7BeH^+$ and $^7Li^+$ at central density of 10^{13} m^{-3}. Note there are two types of modes of oscillations. There are slow "diocotron" modes and fast "cyclotron" modes. Note that we do not observe any even angular m order modes because of the symmetry of our detection.

SIMULATING THE FTICR-MS SIGNAL IN A 2D PIC CODE

3.1 INTRODUCTION AND OVERVIEW OF CODE OPERATION

^{7}Be and ^{7}Li ion plasmas were simulated in a collisionless, electrostatic, 2-dimensional particle-in-cell (PIC) code to better understand the FTICR-MS signal in the plasma regime. The FTICR-MS signal is not well understood in this regime. Others have tried to solve this problem analytically, but it is difficult because it is intrinsically nonlinear.

We assume that the particles in our plasma do not collide in a manner that affects their cyclotron frequencies. Our collision time in our system between ions is about 2 ms. The period for our cyclotron motion is about 1 μs. Our ion-neutral collision time is of the order of days. This collision time was calculated by assuming a pressure of 10^{-9} torr and a cross sectional area from a water molecule with a radius of 1 Å in length. As a result we do not need to be concerned about ion-neutral collisions.

We also assume that the cyclotron motion of these particles is independent of the bouncing axial motion in our experimental trap. Our PIC code has a Cartesian computational grid with a circular boundary; consequently the code is called Particle Meshed Ring, PMR. It inherited a linear direct solver for the electrical potential from a fluid code named PEPI written by Ross L. Spencer.

PMR begins by inputting the system parameters from an input file which is piped into the program. Next it sets up the storage for the direct Poisson solver, `predir`, and detector, `predetect`. Then it sets up the initial plasma equilibrium. It creates an equilibrium density profile, `dens`, using `deqmaker` and a velocity profile, `veq`, using `veqmaker`. It can also read in an initial perturbed

velocity profile `vrp` into our code to add to the velocity profile `veq` in `veqmaker`. `Partinit` uses `dens` and `veq` to initialize the positions and velocities of each of the particles.

Before entering the main time loop, we initialize our `mover` by taking a half time step backward in our velocities using `vint`. This is done so that we can use the leap-frog method to integrate the equations of motion. The leapfrog method requires the positions and velocities to differ in time by half a timestep. To take this backward step we interpolate the particles' positions on to a computational grid using `densmaker`, apply the initial boundary conditions using `bdycon`, solve Poisson's equation to calculate the electric fields on the grid using `directsolve` and then move this initial half step back by applying Newton's laws of motion to the particles. Thus, we begin our program defining the positions at $t = 0$ and velocities at $t = -\Delta t/2$ for each particle and the initial electric fields, `efg`, on the grid at $t = 0$.

For each time step, the code does the following: (1) It moves each particle subject to the electromagnetic force by interpolating the electric fields on the grid to the particles' positions and using a constant magnetic field perpendicular to the x-y grid using `mover`. (2) It builds a density grid from the particles' positions using `densmaker`. (3) It applies time varying boundary conditions in `bdycon`. (4) It solves Poisson's equation to calculate the electric fields on the grid using `directsolve`. (5) It calculates the induced signal on the wall using `detect`. After the run the induced signal from the wall is post-processed in MATLAB to find the desired FTICR-MS signal.

Figure 3.1 illustrates this overall process. The remaining chapter will cover in detail these main components of our PMR code.
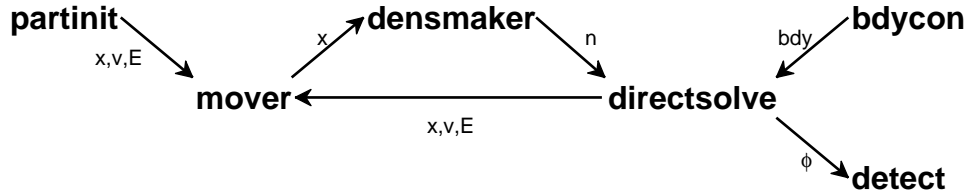
FIG. 3.1 Overview of PMR code. The **bold** text are major subroutines in the code. The small text are the major variables passed from one subroutine to the other. `Partinit` initializes the particles. The middle triangle is the main time loop of the PMR code. The `mover` which moves the particles position and velocities by the Lorentz force. `Densmaker` interpolates the positions to a computational density grid. `Directsolve` solves Poisson's equation to obtain the electric fields. We apply boundary conditions with `bdycon` and detect the signal on the wall with `detect` each time around the time loop.

3.2 PARTINIT: INITIAL PARTICLE DISTRIBUTION

The code begins with an initial dynamical plasma equilibrium. This is accomplished by preparing an initial density profile *dens* and a velocity profile *veq* for `partinit`.

Deqmaker makes a flat or quadratic radial profile by filling the appropriate values in a density grid *dens* for a given profile. In most of our cases, we use a flat radial profile because we assume our plasma has equilibrated to room temperature.

Next, our Poisson solver `directsolve` solves for the electric fields from the given density profile. After calculating the electric fields, `veqmaker` calculates the initial velocity profile *veq* using the Lorentz force. The following equation

$$-\frac{m\,v_\theta^2}{r} = q\,(E_r + v_\theta\,B_z) \tag{3.1}$$

calculates the θ-component of velocity v_θ. `Veqmaker` can also add a radial perturbation to this equilibrium velocity profile.

`Partinit` begins by integrating the density profile to get the total number of particles. Then

it loops through 2-dimensional spatial and velocity grids. In this triple loop, it first calculates the density value for a given x and y position via bilinear interpolation from the density profile. Second, it uses a 2-dimensional Maxwellian distribution to calculate the distribution value at a given position and velocity. The Maxwellian is calculated as follows:

$$f(x,y,v) = n(x,y) \; \frac{1}{2\pi \; v_{th}^2} \; e^{-\frac{1}{2}(\frac{v}{v_{th}})^2} \tag{3.2}$$

where $v_{th} = \sqrt{\frac{k_B T}{m}}$ is the thermal velocity and $n(x,y)$ is the density value at a given x and y position on the grid. Third, it calculates the fraction of simulated particles for a given velocity as follows:

$$\frac{\iint f(x,y,v) \; 2\pi v \; dv \; dA}{N_{tot}} \; n_p = f_v \; n_p \tag{3.3}$$

where f_v is the fraction of real particles for a given velocity and n_p is the number of simulated particles. Then `partinit` uses a random number generator to place the simulated particle's position and velocity randomly in the given position and velocity bin. Next we add the equilibrium velocity profile to this initial thermal velocity distribution. Finally, we calculate *sizepart*, the ratio of the number of real physical particles to simulated particles to be used throughout the main program.

3.3 MOVER: BORIS-BUNEMAN MOVER

We move each particle using a Boris-Buneman $\mathbf{E} \times \mathbf{B}$ mover. First, this subroutine interpolates the electric field on the grid to the particles' position. It uses the same bilinear weighting that is used in `densmaker`. For the *x*-component of the electric field, we interpolate as follows:

$$E_x(x,y) = f_{00} \; E_x(i,j) + f_{10} \; E_x(i+1,j)$$
$$+ f_{01} \; E_x(i,j+1) + f_{11} \; E_x(i+1,j+1) \tag{3.4}$$

where f_{xx} are weights from each quadrant of the cell. Figure 3.3 illustrates these area weights.

Second, it moves the particles according to a Boris mover.[33] This mover is based on a leap-frog scheme. Using the following centered-difference form of the Lorentz equations of motions:

$$\frac{\mathbf{v}_{t+\Delta t/2} - \mathbf{v}_{t-\Delta t/2}}{\Delta t} = \frac{q}{m}\left[\mathbf{E} + \frac{\mathbf{v}_{t+\Delta t/2} + \mathbf{v}_{t-\Delta t/2}}{2} \times \mathbf{B}\right] \tag{3.5}$$

we move each particle forward in time. This mover separates the electric and magnetic forces. Initially each particle experiences a half time step from the electric force:

$$\mathbf{v}^- = \mathbf{v}_{t-\Delta t/2} + \frac{q\mathbf{E}}{m}\frac{\Delta t}{2}. \tag{3.6}$$

This is followed by a rotation from $\mathbf{v}^-$ to $\mathbf{v}^+$ by the magnetic force using Buneman's[34] reduced set of equations:

$$v_x' = v_x^- + v_y^- \tan(\theta/2) \tag{3.7}$$

$$v_y^+ = v_y^- - v_x' \sin(\theta) \tag{3.8}$$

$$v_x^+ = v_x' - v_y^+ \tan(\theta/2). \tag{3.9}$$

Here, $\theta = \omega_c \Delta t = \frac{qB}{m}\Delta t$ is the cyclotron angular frequency multiplied by the time step. Then we calculate the remaining half time step from the electric force:

$$\mathbf{v}_{t+\Delta t/2} = \mathbf{v}^+ + \frac{q\mathbf{E}}{m}\frac{\Delta t}{2}. \tag{3.10}$$

Finally, we conclude by moving the particle's position as follows:

$$\mathbf{x}_{t+\Delta t} = \mathbf{x}_t + \mathbf{v}_{t+\Delta t/2}\Delta t. \tag{3.11}$$

For more information about this Boris-Buneman mover see Birdsall's[35] text.

Lastly the `mover` checks to see if the particle has escaped from our allowable computational region. Figure 3.2 illustrates this process. The particle array is ordered in such a way that all species 1 particles are together followed by all species 2 particles and so forth. The escaped particles are placed in the end of the active part of this particle array. As a result, it is important that the order of this particle array is maintained as `mover` moves the escaped particles to the end of the particle array.

The basic algorithm is that if a particle escapes the computational region, we decrement the number of active particles and increment the number of escaped particles. If the current particle has not escaped, the next time through the loop, we exchange the current value with the value at the number of escaped particles position. Figure 3.2 illustrates this in the fifth iteration where the current position 5 in the array is exchanged with position 3 in the array because there are 2 escaped particles. In short, this algorithm is efficient only because it maintains the particle array order and does not need to shift the remaining array up each time a particle escapes.

3.4 DENSMAKER: PARTICLE POSITIONS TO DENSITY GRID

`Densmaker` makes a density grid $\rho_{i,j}$ from the particles' positions $p(x,y)$. The density is described by a cell-edge grid as shown in Fig. 3.3. First consider the x-direction. We begin by calculating the particle's distance from the edge of the grid x_i in terms of the grid spacing dx. This is calculated as follows:

$$x_l = \frac{x - x_i}{dx} + 1.$$ (3.12)

This dimensionless value is only an integer when the particle's position is on a grid point. We next truncate this factor x_l to be an integer in order to get the left grid index i_l. To obtain the fraction of the cell in the x-direction, f_x, we take the difference of this particle distance x_l and the left grid
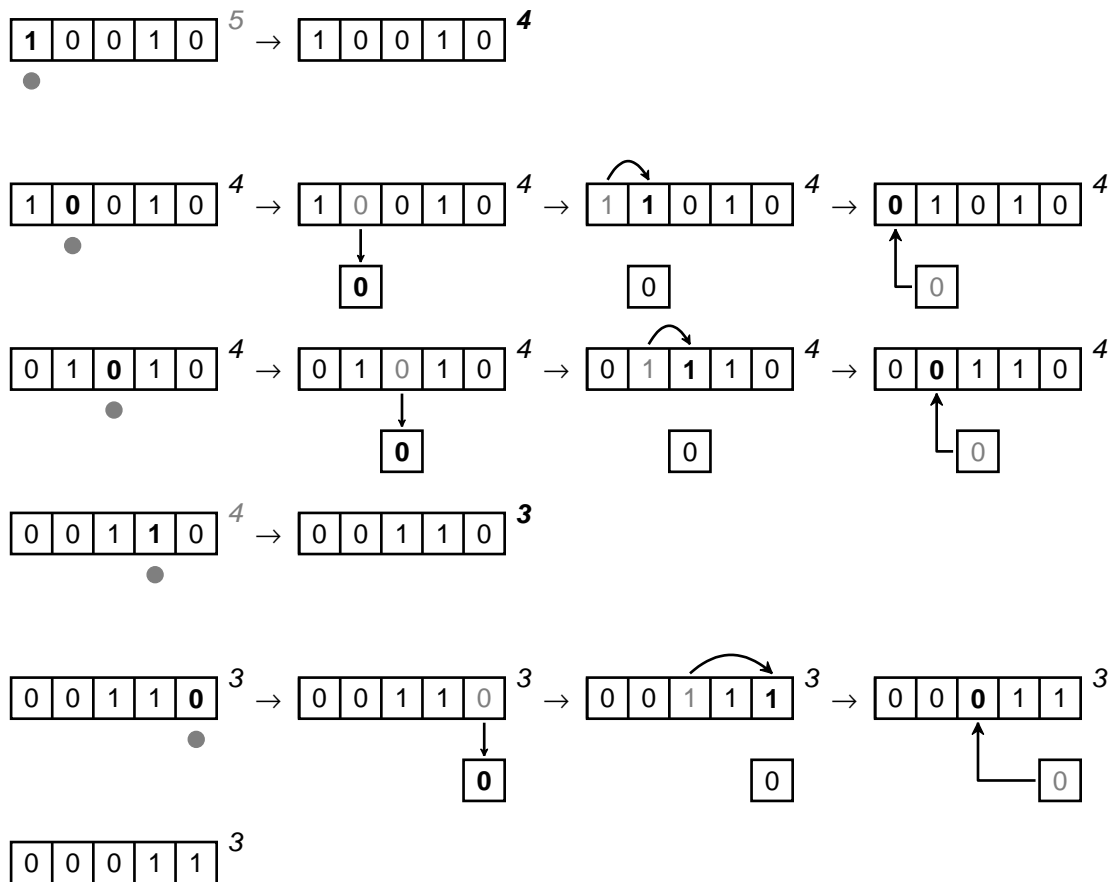
FIG. 3.2 This is a workflow cartoon of how escaped particles are moved to the end of the particle array. Each row represents one iteration in the for loop stepping through the particle array. Each column represents one step in each iteration. The dot in the first column represent the current element on the array for that iteration. The extra box in the second, third and fifth rows represents a temporary variable. The number on the upper right corner represents the number of active particles. The bolded values represent the current affected value. The value of one represents a particle that has escaped the allowable computation region.
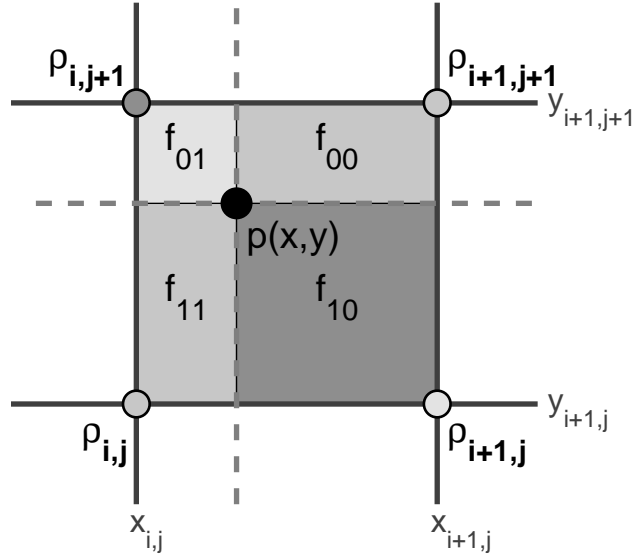
FIG. 3.3 Accumulation of fraction of density unto grid points ρ by opposing area f. The density grid point $\rho_{i,j}$ accumulates the fraction of density from the area is f_{00} for particles' position at $p(x,y)$.

index i_l. By construction this fraction is always positive. We then find the analogous values in the y-direction.

After obtaining these fractions for both directions, we calculate the weights for the four corners of the cell. For the left-bottom corner, the weight f_{00} is the area $(1 - f_x)(1 - f_y)$ times grid density factor f_0. This is the area of the region opposite to the left-bottom grid point as shown in Fig. 3.3. The grid density factor f_0 is just the grid density $1/dx^2$ which has units m^{-2}.

3.5 BDYCON: EXCITE CYCLOTRON MOTION BOUNDARY CONDITIONS

To excite the cyclotron motion of each species, we apply an oscillating electric potential on two sectored boundaries. The two sector boundaries are out of phase with each other.

Bdycon applies these boundary conditions by first setting the functional form of the electric potential. It can apply a grounded condition, an impulse, single frequency excitation, broadband

excitation, or read a file of the functional voltage form. It continues to apply this form until the driving time t_{dr} is reached. Bdycon uses a function phibdy to calculate the boundary value for a given angular value. Phibdy also sets up the two left and right quarter sector boundaries on which we apply these conditions. It also sets the value on one sector opposite to that of the other.

For the grounded condition, bdycon sets all the boundary values to zero voltage. For the impulse condition, it sets the boundary values to a constant voltage. For the single frequency excitation, it sets the boundary values to a sinusoidal function with a driving amplitude A and a single driving frequency ω.

For broadband excitation, we use the following functional form:

$$f(t) = a\, t_{dr}\frac{sin(\omega_1 \tau) - sin(\omega_2 \tau)}{\pi\,\tau} \tag{3.13}$$

where a is the spectral amplitude, t_{dr} is the driving time, ω_1 is the start angular frequency, ω_2 is the end angular frequency, and $\tau = t - .5\, t_{dr}$. This functional form is analogous to a bandpass filter. This functional form and its spectrum is illustrated in Fig. 3.4. In the time domain, its maximum amplitude from base to peak can be calculated as follows:

$$A_{max} = 2\, t_{dr}\sum_n^N a_n \Delta_n \tag{3.14}$$

where A_{max} is the maximum time amplitude, Δ_n is the bandwidth of the rectangular function, and the sum is over N number of rectangular functions in the spectrum.

If we read a file for the functional voltage waveform, bdycon linearly interpolates this voltage form in time. One standard voltage waveform we read from a file is the optimized stored waveform inverse Fourier transform (SWIFT) waveform. This excited waveform and its spectrum is illustrated Fig. 3.5.
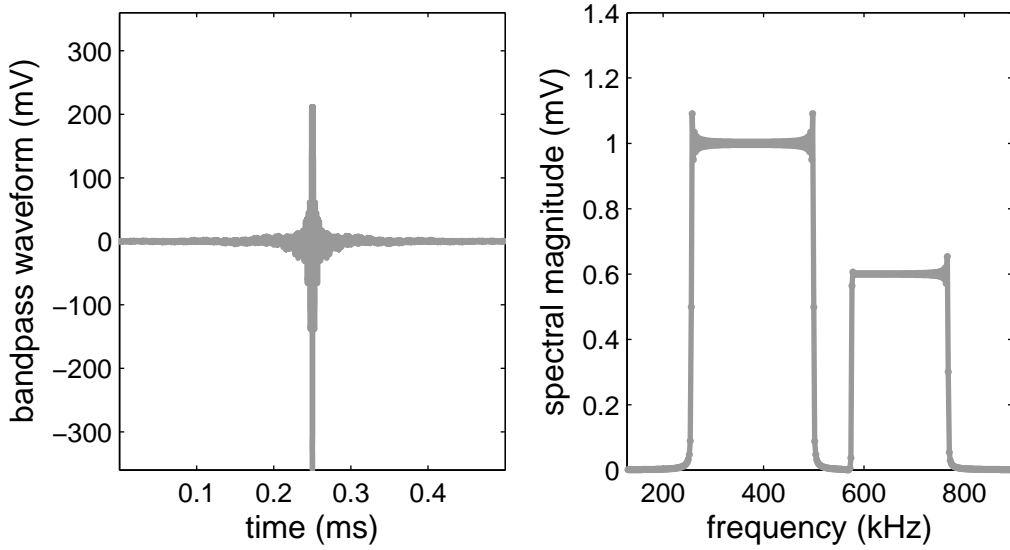
FIG. 3.4 Bandpass filter time and frequency domain. Note the high dynamic range that would be required in the time domain (about 800 mV). Note the Gibb's phenomena on the edges of the rectangular profiles in the frequency domain.

SWIFT was first developed by Marshall *et. al.*[36] This technique involves inverse Fourier transforming a desired excitation magnitude spectrum $F(\omega)$ to excite the cyclotron motion of the ions in FTICR-MS trap. Subsequently, Chen *et. al*[37] found that any nonlinear phase modulation (preferably a quadratic phase function) reduced the dynamic range in the time domain. Later, Guan and McIver[38] developed a optimized quadratic phase function. We have used their optimized phase function.

Guan and McIver's optimal phase function $P(\omega)$ is calculated using the desired power spectrum $G(\omega) \equiv |F(\omega)|^2$ as follows:

$$P(\omega) = \frac{t_1 - t_0}{\int_{\omega_0}^{\omega_1} G(y)dy} \int_{\omega_0}^{\omega} \int_{\omega_0}^{y} G(x)dxdy + t_0(\omega - \omega_0) + P_0. \qquad (3.15)$$

The first term spreads the excitation power over the time period $t_1 - t_0$. The integral $\int_{\omega_0}^{\omega_1} G(y)dy$ is the area under the power spectrum. The second term time shifts the waveform to the time location
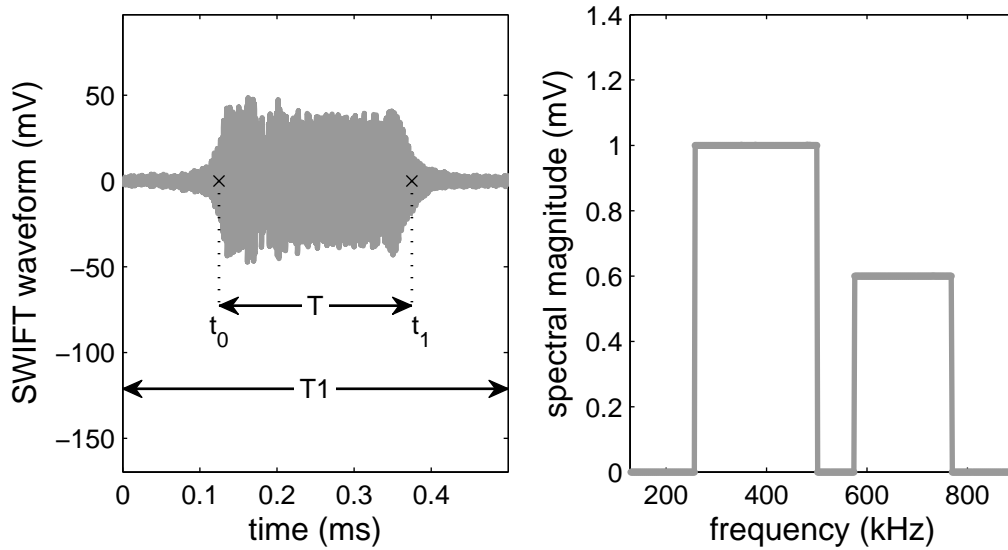
FIG. 3.5 This is stored waveform inverse Fourier transform (SWIFT) time and frequency domain. The techniques involves using a desired excitation magnitude spectrum (like the one on the right) to obtain the time domain signal on the left. The time domain has a reduce dynamic range (about 100 mV) compared to the bandpass filter version (about 800 mV) for the same excitation magnitude spectrum. Note the frequency domain does not exhibit the Gibb's phenomena on the edges of the rectangular profiles.

between t_0 and t_1. The third term is the initial phase P_0 which we can simply choose to be zero.

If we choose to spread our excitation power to half the excitation time T_1, this phase function can be reduced in the following way. First let us define the time period over which we spread the excitation power as

$$T \equiv t_1 - t_0 = T_1/2.$$

Second, we define the starting point of this excitation spread as

$$t_0 \equiv (T_1 - T)/2 = (T_1 - T_1/2)/2 = T_1/4.$$

Now, we discretize our continuous integrals into sums as follows:

$$P_k = \frac{T_1}{2 \sum\limits_{k=1}^{N-1} G_k} \sum_{j=1}^{k} \sum_{i=1}^{j} G_i \Delta\omega + \frac{T_1}{4} k \Delta\omega$$

The double sums are cumulative sums. Then, we note how the sampling frequency f_s is related to our excitation interval T_1, angular frequency step $\Delta\omega$, and its product as follows:

$$\left.\begin{array}{l} T_1 = N\Delta t = N\dfrac{1}{f_s} \\[2ex] \Delta\omega = 2\pi\Delta f = 2\pi\dfrac{f_s}{N} \end{array}\right\} \quad T_1\Delta\omega = 2\pi.$$

Our phase function reduces to the following form:

$$P_k = \frac{\pi}{\sum\limits_{k=1}^{N-1} G_k} \sum_{j=1}^{k} \sum_{i=1}^{j} G_i + \frac{\pi}{2} k$$

For a phase function of frequency rather than angular frequency, we can divide the top form by 2π to get the following:

$$P_k' = \frac{P_k}{2\pi} = \frac{1}{2 \sum\limits_{k=1}^{N-1} G_k} \sum_{j=1}^{k} \sum_{i=1}^{j} G_i + \frac{1}{4} k$$

3.6 DIRECTSOLVE: SOLVE POISSON'S EQUATION FOR ELECTRIC FIELDS

We solve Poisson's equation using a matrix solver. We translate Poisson's equation $\nabla^2 V = -\rho/\varepsilon_0$ into the linear problem $Ax = b$. We finite difference the Laplacian, ∇^2, as follows:

$$\nabla^2 V = \frac{V_{i+1,j} - 2V_{i,j} + V_{i-1,j}}{\Delta x^2} + \frac{V_{i,j+1} - 2V_{i,j} + V_{i,j-1}}{\Delta y^2} = -\frac{\rho}{\varepsilon_0} \tag{3.16}$$

The coefficients in front of the electric potential terms form the matrix A. The right-hand side of Poisson's equation is just the density grid calculated by `densmaker` times a known constant q/ε_0. We are trying to solve for the electric potential which is our unknown matrix x.

To solve for the unknown x, we decompose the invertible matrix $A = LU$ into its lower and upper triangular matrices. This breaks the single matrix problem into two easier matrix problems as follows:

$$A\,x = b \rightarrow \begin{cases} L\,y = b \\ \\ U\,x = y \end{cases} \tag{3.17}$$

We first solve for the unknown y's by forward substitution of the known b's into the lower triangular matrix L. Then we backward substitute the y's into the upper triangular matrix U to solve for the unknown x's.

For our code, we use a cartesian grid with a circular boundary to avoid the difficulties at the origin in polar coordinates. `Presor` prepares the storage for both the direct linear solver, `directsolve`, and the FTICR-MS detection subroutine, `detect`. It first identifies the interior points. Each interior point is a point surrounded by four other grid points which are inside the circular boundary. Then it identifies the edge points which are the outer edge grid points surrounding the interior grid points. These edge points are the closest grid point to the boundary. `Presor` also calculates the scaled lengths from the edge points to the circular boundary. Figure 3.6 illustrates these points and lengths.

`Predir` loads a banded matrix A with the appropriate coefficients for the Laplacian operator. It starts by loading the normal center-difference coefficients from the Laplacian operator as shown in Eq. 3.16. Then it loads the identity operator for the points outside our circular boundary. For our circular boundary, it quadratically extrapolates the Laplacian operator for each direction, adding the appropriate coefficients together.
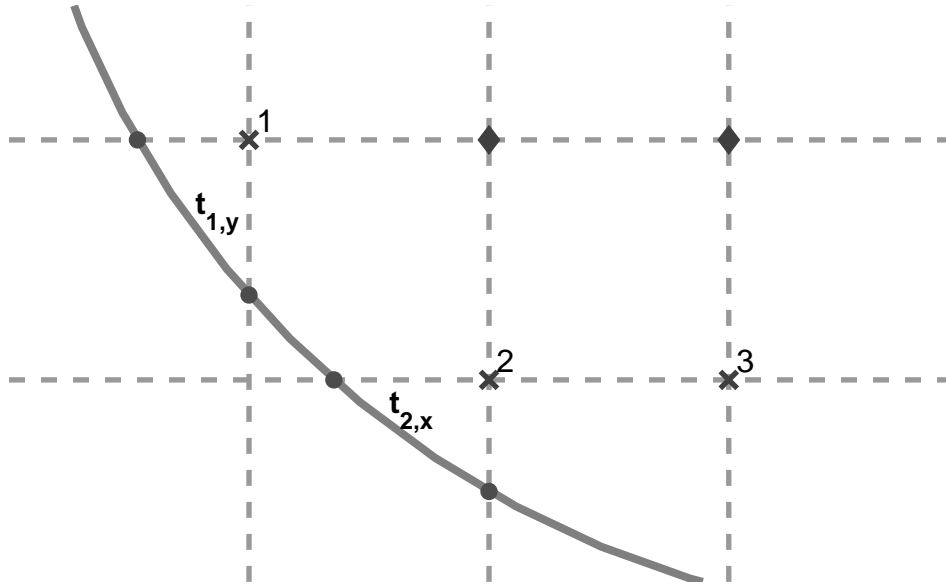
FIG. 3.6 The computation grid to solve Poisson's equation. The interior points are mark by diamonds. The edge points are mark by "X"'s. The boundary points are mark by circles. $t_{1,y}$ and $t_{2,x}$ are the scaled distance from the edge point to the boundary point.

For a south-west edge point, the extrapolated Laplacian operator is as follows:

$$\nabla^2 V_{i,j} = \frac{2}{\Delta x^2} \left[\frac{V_{1,x}}{t_{1,x}(t_{1,x}+1)} - \frac{V_{i,j}}{t_{1,x}} + \frac{V_{i+1,j}}{t_{1,x}+1} \right]$$

$$+ \frac{2}{\Delta y^2} \left[\frac{V_{1,y}}{t_{1,y}(t_{1,y}+1)} - \frac{V_{i,j}}{t_{1,y}} + \frac{V_{i+1,j}}{t_{1,y}+1} \right] = -\frac{\rho}{\varepsilon_0}. \quad (3.18)$$

where $V_{1,x}$ and $V_{2,x}$ are the electric potential values on the circular boundary, $t_{1,x}$ and $t_{1,y}$ are the scaled length from the edge point to the circular boundary, and Δx and Δy are the grid spacings in the respective x and y directions. Figure 3.7 shows how this operator can be visually described as a "short-legged" operator where $t_{1,x}$ and $t_{1,y}$ are the short legs compare to the normal grid spacing Δx and Δy. `Predir` also loads the coefficients from the boundary terms like $V_{1,x}$ and $V_{2,x}$ that contribute to the right-hand side of the problem. These coefficients will be combined in `directsolve` with the boundary conditions from `bdycon` to build the proper right-hand side of the equation.
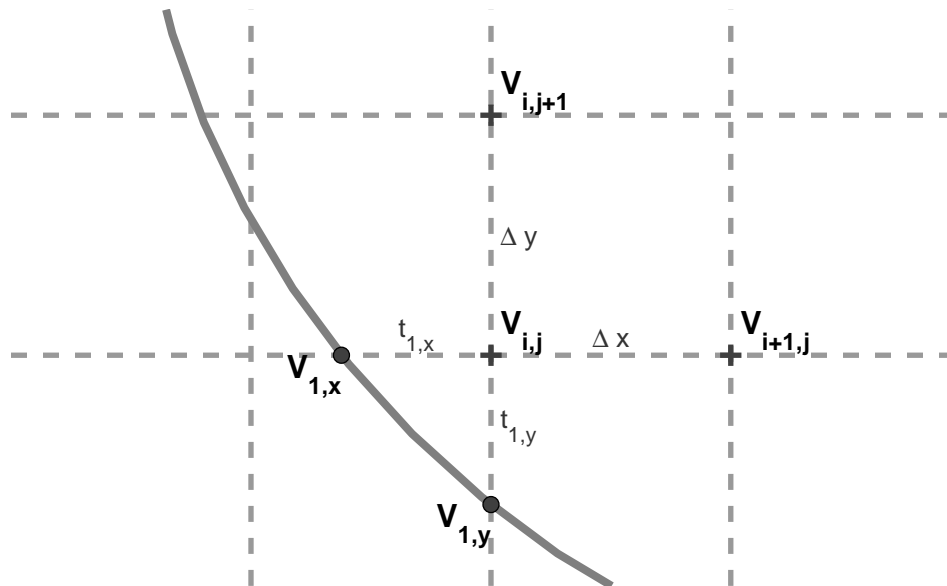
FIG. 3.7 Southwest short-legged operator for circular boundary. This operator is a quadratic extrapolation of the normal Poisson operator. Notice the "short" legs of this operator are $t_{1,x}$ and $t_{1,y}$ in contrast to the "normal" legs Δx and Δy.

Finally, `predir` decomposes this banded matrix A into lower and upper triangular matrices using the subroutine `ludcmp_b`. In our code, the decomposed banded matrix A_{LU} replaces the original banded matrix A. Note that this decomposition only needs to be done once, since A only depends on the type of boundary conditions at the wall and not in the value of the boundary condition.

   `Directsolve` first loads the density part from `densmaker` to the right-hand side of the matrix equation. Second it adds the boundary conditions to the right hand side. This involves multiplying the operator coefficients calculated by `predir` with the boundary values from `bdycon`. Then it directly solves for the electric potential by doing the forward substitution for the lower triangular matrix and back substitution for the upper triangular matrix using the subroutine `lubksb_b` on the banded matrix A and right-hand side contribution. Finally, we use these electric potential values to calculate the electric fields for each direction on the grid. For more information about how to solve Poisson's equation, I refer to Birdsall's[35] and Hockney's[39] texts.
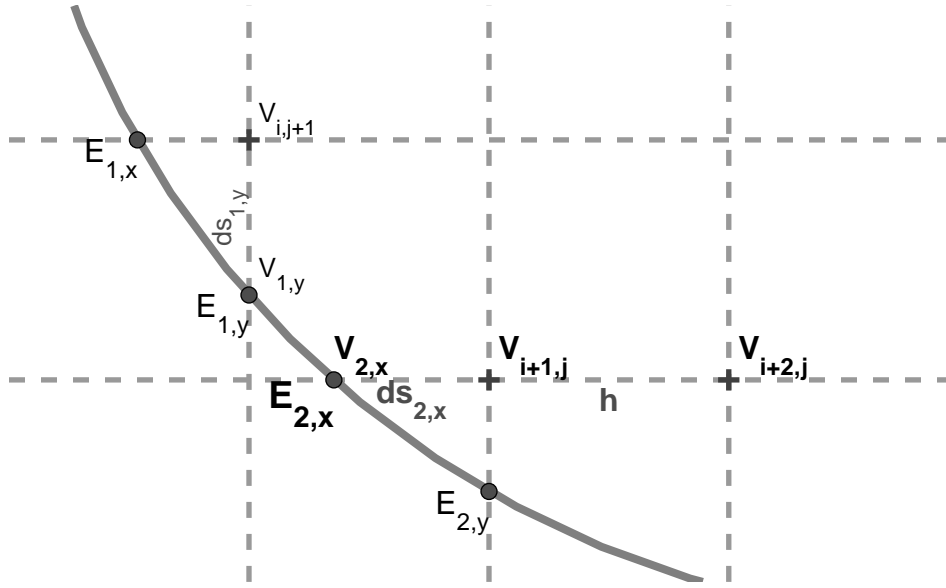
FIG. 3.8 To extrapolate x-component of the electric field on the boundary point $E_{2,x}$, we use the electric potential values on the boundary point $V_{2,x}$ and the grid points $V_{i+1,j}$ and $V_{i+2,j}$. We also use the distances $ds_{2,x}$ and h. We quadratically extrapolate the electric field to the boundary.

3.7 DETECT: CALCULATE THE WALL SIGNAL

To detect our signal, we calculate the electric field at the boundary using the electric potential at the boundary and two nearest interior grid points. Figure 3.8 shows how we quadratically extrapolate the electric field to the boundary. In the x-direction, the equation for the electric field is as follows:

$$E_{2,x} = -\frac{\partial V_{2,x}}{\partial x} = \frac{2ds_{2,x}+h}{ds_{2,x}\,(h+ds_{2,x})}V_{2,x} - \frac{h+ds_{2,x}}{ds_{2,x}\,h}V_{i+1,j} + \frac{ds_{2,x}}{(h+ds_{2,x})\,h}V_{i+2,j} \qquad (3.19)$$

where $ds_{2,x}$ is the distance from the edge grid point to boundary and h is the grid spacing in the x-direction. We use the boundary point $V_{2,x}$ and the two nearest interior points $V_{i+1,j}$ and $V_{i+2,j}$ to extrapolate $E_{2,x}$ on the boundary.

As one can notice from Fig. 3.8, we will not get both components of the electric field at each boundary point. Also, they will not be equally spaced in angle on the boundary arc. So, we

interpolate the extrapolated electric field components to a uniformly spaced angle array.

`Predetect` prepares indices and coefficients to quadratically extrapolate the electric field to the circular boundary. It also creates a sorting key to sort these values by increasing angle value. Then it calculates the indices and coefficients to cubically interpolate onto a uniform angle grid. `Predetect` also maintains the angle periodicity such that when it passes $-\pi$ or π, the values are mapped back onto the values between $-\pi$ to π

`Detect` uses the preparation from `predetect` to calculate the induced charge on a boundary sector. It extrapolates the electric field on the boundary, sorts them by increasing angle value, and interpolates them onto a uniform-spaced arc grid. Then, we numerically integrate the electric fields on each boundary arc using a composite Simpson's algorithm to calculate the induced line charge on them. This algorithm is as follows:

$$\lambda = r_b \, \varepsilon_0 \frac{\Delta\theta}{3} \left[E_r(\theta_0) + 4 \sum_{m=1,3,\dots}^{N} E_r(\theta_m) + 2 \sum_{n=2,4,\dots}^{N} E_r(\theta_n) \right] \tag{3.20}$$

where r_b is the radius to the boundary, ε_0 is the permittivity of free space, $\Delta\theta$ is the uniform grid spacing, E_r is the electric field on the uniform arc, and N is the total number of values between the first and final angles. Finally, we subtract this time signal from the opposing sectors to obtain the wall signal.

To verify that our `detect` was working properly, we compared the simulation results for the electric fields on the wall with an analytical solution for the radial electric field from a line charge in a grounded infinite cylindrical wall. The analytical solution we use is as follows:

$$E_r = \frac{\lambda}{2\pi\varepsilon_0 r} \frac{(r^2 - r'^2)}{(r^2 - 2rr'cos(\theta - \theta') + r'^2)} \tag{3.21}$$

where the primed variables (r', θ') relate to the distance and angle to the line charge and the un-

primed variables (r,θ) to the boundary wall. Figure 3.9 illustrates this analytical solution. As a line

charge moves closer to the wall, the peak height increases. As the line charge rotates to a different

angle, the peak occurs at that given angle. We also checked that the integrated values of the electric

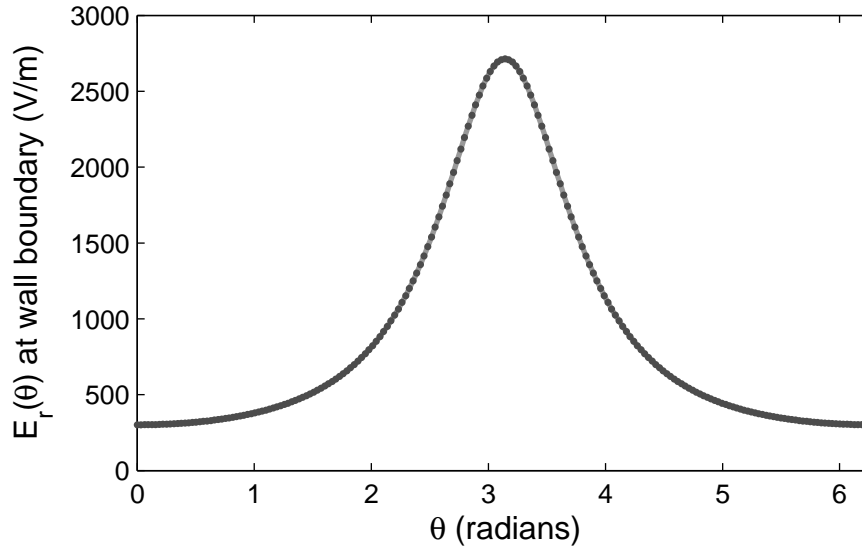field are the same as the analytical solution.

FIG. 3.9   Radial electric field at the wall boundary for a line charge at $(R,\theta) = (0.02 \text{ m}, 180°)$. As the line charge moves closer to the wall, the peak height increases. As the line charge rotates to a different angle, the peak occurs at that given angle.

3.8 MATLAB ANALYSIS

After obtaining the wall signal from the 2D PIC simulation, we post-process this signal in MAT-

LAB to obtain our desired FTICR-MS spectrum. The 2D PIC code writes out the time and the

difference of the induced line charge on two opposing sectors to a text file.

In a MATLAB script, we first read this file and convert this wall signal $\Delta\lambda(t)$ into voltage

signal $v(t)$ as follows:

$$v(t) = \Delta\lambda(t)\frac{L}{C} \tag{3.22}$$

where C is the capacitance and L is the length of the ring electrode. For our 8 mm electrode, the capacitance is about 85 pF.

We fast Fourier transform (FFT) our voltage signal to obtain the magnitude and phase spectrum. A good review on this material can be found in the MATLAB help and National Instruments LabVIEW 2009 Help. FFT is the algorithm which gives the discrete Fourier transform (DFT) of the time signal. The DFT and its inverse are defined as follows:

$$X_k = \sum_{n=0}^{N-1} x_n \, e^{-i\frac{2\pi k}{N}n} \qquad \Leftrightarrow \qquad x_n = \frac{1}{N}\sum_{k=0}^{N-1} X_k \, e^{i\frac{2\pi k}{N}n} \tag{3.23}$$

where x_n represents the sample time signal and N is the total number of samples. Both the time domain x_n and the frequency domain X_k have a total of N samples. X_k is a sequence of complex numbers which represents the amplitude and phase of different sinusoidal components of the discrete time signal x_n. The normalization constant 1 and $1/N$ in front of these transformations and the sign in the exponent are chosen by convention.

We can rewrite the argument of the exponent as follows:

$$i\,2\pi k\,\frac{1}{N}\,n = i\,2\pi k\,\frac{f_s}{N}\,n\frac{1}{f_s}$$
$$= i\,2\pi k\,\Delta f\,n\Delta t$$
$$= i\,\omega_k\,t_n.$$

First, we multiply the numerator and denominator by the sampling frequency, f_s. Second, we note how f_s is related to the frequency step, Δf, and time step, Δt. Third, we note how Δf and Δt are related to the discrete frequency values, ω_k, and discrete time values, t_n.

$$x_n = \frac{1}{N}\sum_{k=0}^{N-1} X_k \, e^{i\omega_k t_n} \qquad \Leftrightarrow \qquad X_k = \sum_{n=0}^{N-1} x_n \, e^{-i\omega_k t_n}$$

Now the inverse DFT states that the discrete time signal x_n can be made up of a sum of sinusoidal components $e^{i\omega_k t_n}$ with a given complex amplitude X_k. In this form, we can see that the DFT is a truncated exponential Fourier series. The DFT is also a series of delta functions spaced by the time interval $\Delta t = 1/f_s$.

The first term in the DFT of a time signal X_0 is the average value or DC component of the signal. For a constant time signal with 4 samples of 1 V, this would be 4 V. To normalize this, we divide this term by the total number of samples to get back 1 V.

The spectral magnitude of our signal is the amplitude of X_k in polar form. We calculate this magnitude by taking the complex modulus of X_k and multiplying by the normalization constant $1/N$ as follows:

$$a_k = \frac{|X_k|}{N} = \frac{\sqrt{\mathrm{Re}(X_k)^2 + \mathrm{Im}(X_k)^2}}{N}. \tag{3.24}$$

For real time values x_n, X_k is related to X_{N-k} as follows:

$$X_k = X_{N-k}^* \tag{3.25}$$

where the star denotes complex conjugation. As a result of this relation, our spectrum is half redundant and we usually only look at half the spectrum. However, the amplitude of this half spectrum is only half the value. Therefore, to obtain the absolute amplitude of the sinusoidal components, we need to multiply our spectral magnitude by 2. A spectrum displayed this way is usually referred to as a one-sided or single-sided spectrum. Since we are looking at relative amplitudes, we have ignored this factor of 2 in our spectra.

If the number of samples N is even, then there is a value at the Nyquist frequency. The Nyquist frequency is half the sampling frequency. Below the Nyquist frequency are the positive frequencies. Above the Nyquist frequency are the aliased negative frequency components. If the signal

has frequency components above the Nyquist frequency, then these components spill over to the positive frequencies. This phenomena is called *aliasing* where we can not distinguish the alias frequencies from the actual frequencies in the signal.

To avoid this problem, the Nyquist frequency needs to be greater than the highest frequency in our signal.

$$f_N = \frac{f_s}{2} > f_{max} \tag{3.26}$$

For our case, the Nyquist frequency is about 4 MHz which is greater than the highest frequency component in our signal which is at 1 MHz.

The DFT of a time signal assumes periodicity with a period length of N. In most applications of DFT, we truncate a time signal with an incomplete number of cycles. This causes the DFT signal to leak amplitude from the actual frequency to other frequencies. This phenomena is known as *spectral leakage*. To resolve this issue, we use a technique known as *windowing* where we artificially constrain the signal to be narrow in time. As we narrow the signal in time, it broadens the spectral peaks so that they don't fall to other finite frequency values. We window our signal by multiplying it by a given window function.

In our case, we use a Hann window to resolve this issue. The Hann window function is defined as:

$$w(n) = 0.5 \left[1 - \cos\left(\frac{2\pi n}{N-1} \right) \right]. \tag{3.27}$$

The bottom left plot in Fig. 3.10 shows how the Hann window narrows the raw time signal. The windowed spectral magnitude at the bottom right illustrates that we do not actually have a peak point. It also does not allow any spectral leakage to other frequencies as the raw spectral magnitude does in the above right plot in Fig. 3.10.

Goodner *et. al*[40] did an extensive study on quantifying the ion abundances in FTICR-MS. Based on their results, in order to obtain an optimal quantization of the spectrum they recom-
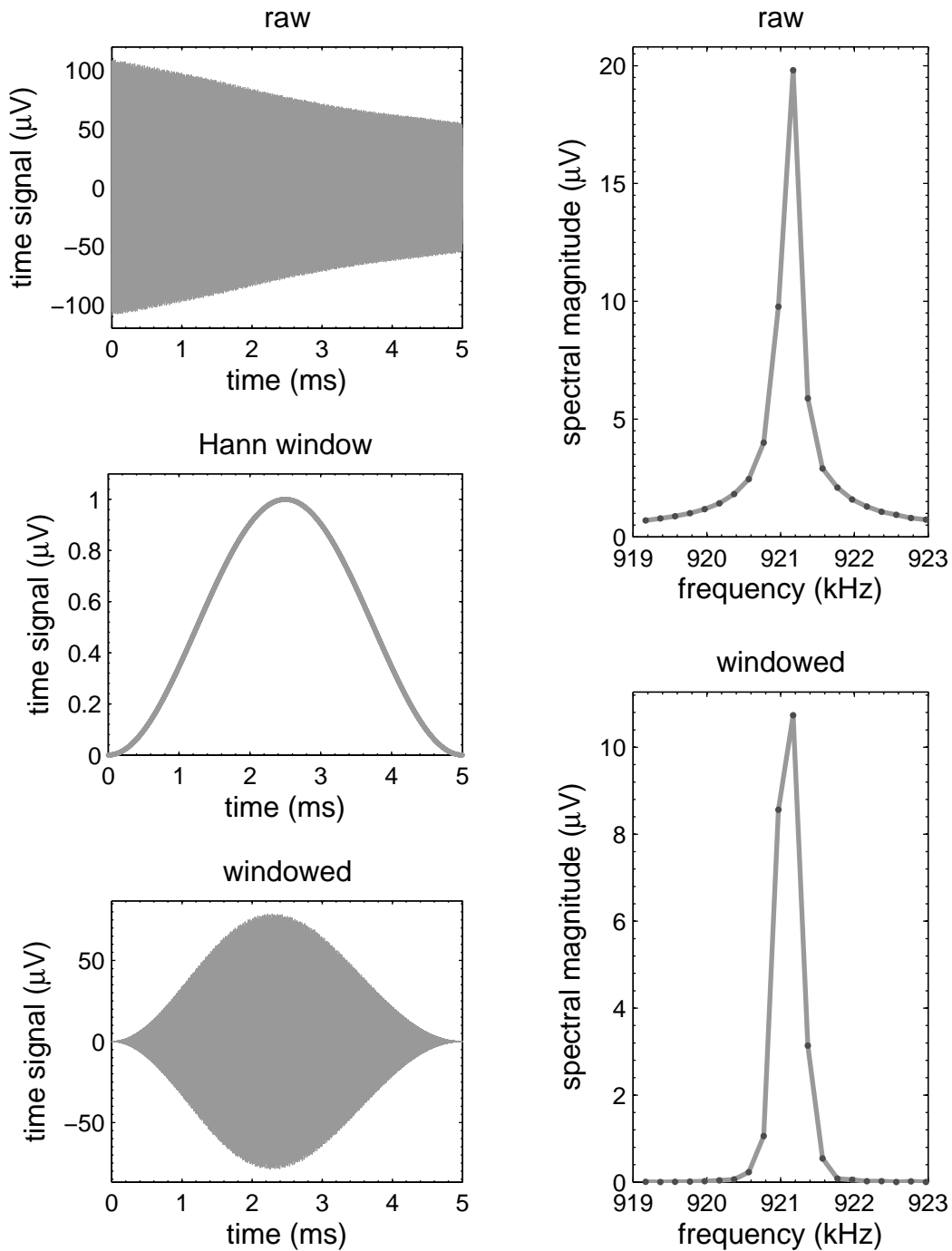
FIG. 3.10 Comparison of Hann windowed signal vs. raw signal. On the left column, we show the raw time signal, the Hann window, and the windowed signal. On the right column, we illustrate the raw spectrum and the windowed spectrum. The windowed spectrum does not have the spectral leakage seen in the raw spectrum.

mended the following: (1) Use the appropriate window or apodization function for peak height ratios observed in the spectrum. (2) Zero fill the time signal until the peaks of interest are represented by 10-15 points. (3) Use three data points of highest intensity of the peak to locate the peak maximum by fitting it to a polynomial of the form $y = (ax^2 + bx + c)^n$. In this peak fitting procedure, they use what Goodner *et. al* termed as "Comisarow method"[41] which is to use an appropriate n for the apodization function. They also found that the accuracy of quantitation using peak height is about equal to that of peak area measurements.

For analysis of our spectra, we chose to use a Hann window to resolve relative ratios of about 1 to 10 for peak height measurements. We also took Goodner *et. al*'s other suggestions and tested them on our known $^7\text{Be}^+$ and $^7\text{Li}^+$ plasma at a density of 10^9 m^{-3}. In order to locate the peak maximum and frequency, we found that the best peak fitting function was a Comisarow polynomial of form $y = (ax^2 + bx + c)^n$ where $n = 5.5$ for a Hann window. Zero filling was not helpful so we used the raw windowed time signal in our analysis. To find the area under the spectral peak, we use a trapezoidal method.

3.9 VERIFYING OUR 2D PIC CODE

To verify our 2D PIC code, we first calculated the diocotron frequency for the single species plasma and compared it to the analytical solution for an infinitely long plasma:

$$\omega_d = \frac{\omega_p^2}{2\omega_c} \frac{R_p^2}{R_w^2} = \frac{en_0}{2\varepsilon_0 B_z} \frac{R_p^2}{R_w^2} = \frac{\lambda}{2\pi\varepsilon_0 R_w^2 B_z} \tag{3.28}$$

where ω_d is the diocotron angular frequency, λ is the charge per length, R_w is the radius to the wall, and B_z is the axial magnetic field strength. The diocotron frequency for an infinitely long ^7Be ion plasma with a central density of 10^{13} m^{-3} is 8.359 kHz. The plasma radius R_p is about

2 cm and the confining wall radius R_w is 4 cm. Note the line charge density was calculated in the simulation by taking the number of real particles per length multiplied by the elementary charge. The line charge density λ was calculated to be 2.01 nC/m for this simulation run.
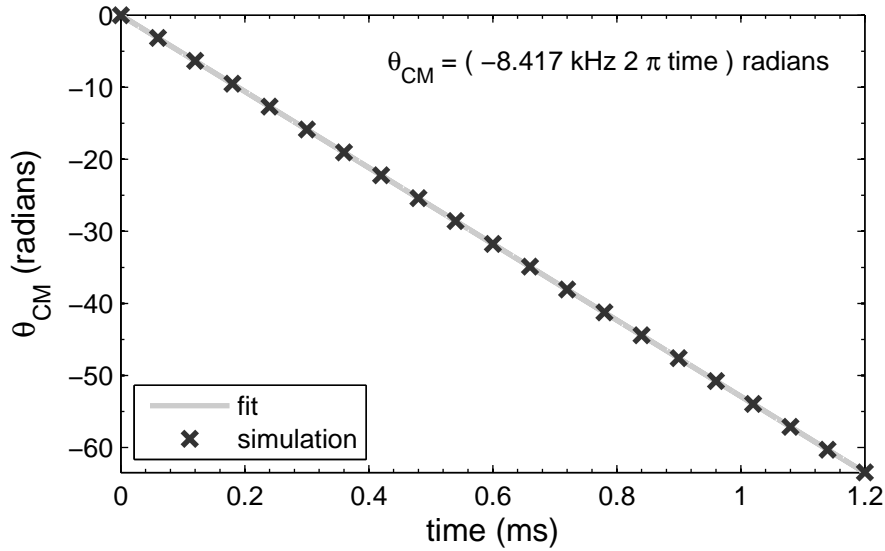

FIG. 3.11 This is a linear fit of the center-of-mass angle θ_{cm} for a ^{7}Be ion plasma with a density of 10^{13} m^{-3} and a 1 mm x-offset from the axis. The fitted diocotron frequency for an infinitely long plasma is 8.417 kHz. The fitted equation is written in the top right corner.

In our code, we initially shifted our plasma column using a 1 mm offset in the x direction from the axis. We observed the center-of-mass motion for about 10 cycles of diocotron period. Finally, we fitted the center-of-mass angle θ_{cm} to a line and compared its slope to the infinite analytical solution given by Eq. 3.28. Figure 3.11 shows that our simulation agrees with the analytical solution to within 0.689%. The fitted diocotron frequency for our infinitely long plasma is 8.417 kHz.

To understand how the time step influences our frequency measurement, we performed FTICR measurements in our code using different time steps in our plasma dynamics. We fast Fourier transformed the signal and fitted the spectral peaks using Goodner's suggest fitting function as discussed previous section. Figure 3.12 illustrates how the time step Δt changes the measured
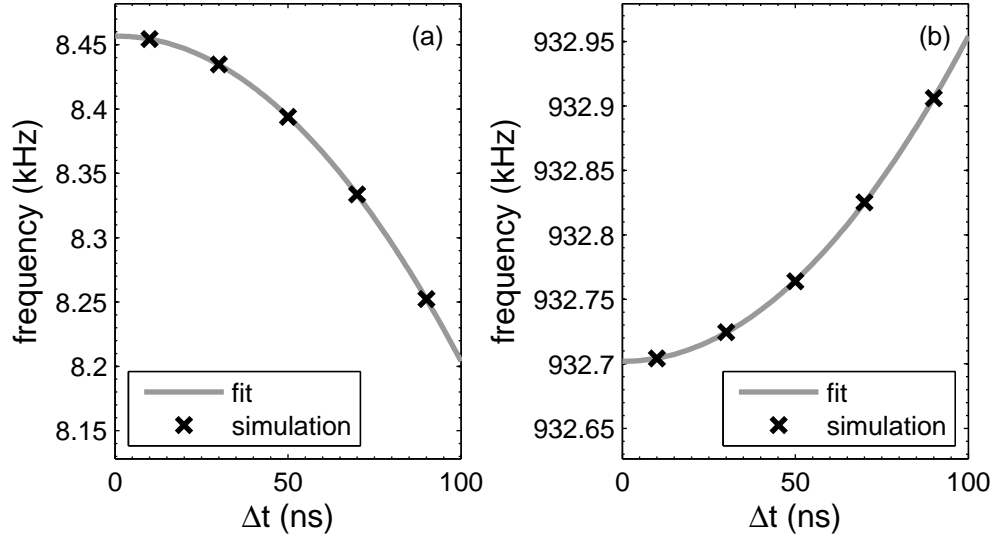
frequencies quadratically.

FIG. 3.12 This is a parabolic fit of the time step Δt to the two characteristic frequencies from the wall signal for a ^{7}Li ion plasma with a density of 10^{13} m^{-3}. The ion plasma was excited with a broadband pulse covering 931 kHz to 933 kHz at 2.5 V for 0.1 ms and was observed for 10 ms. The fitted equation for (a) is f = (-0.0256Δt^2 + 0.0307Δt + 8 457) Hz and for (b) is f = (-0.0255Δt^2 - 0.0240Δt + 932 702) Hz.

For our typical simulation run, we chose to run with a 30 ns time step for a precision of about 4 significant digits in frequency. Notice in Fig. 3.12 (a) the frequency difference between 30 ns time step and ideal 0 ns is downshifted by 22 Hz, while in (b) the frequency difference between 30 ns time step and ideal 0 ns is upshifted by 21 Hz.

To further validate our code we have observed that the total energy is conserved for a non-excited plasma. Also, a plasma initially in equilibrium remains in equilibrium throughout a non-excited simulation run. As result, the PMR code seems to simulate well the physics of a plasma column in an infinitely long grounded cylinder.

We chose our grid spacing to resolve a Debye length. The Debye length, λ_D, is calculated as

follows:

$$\lambda_D = \sqrt{\frac{\varepsilon_0 KT_i}{ne^2}} \tag{3.29}$$

where KT_i is the thermal energy of ions in the plasma and n is the number density. The typical Debye length for our room temperature plasma of densities of 10^{13} m^{-3} is about 377 μm. In our code, we use a 426×426 cell-edge grid covering a space of 8 cm × 8 cm. As a result, our grid spacing of 188 μm is about half a Debye length. At a coarser grid, the damping of the wall signal decreases which is shown in Fig. 3.13. The damping of the signal probably occurs from nonlinear interactions between the two different mass species.
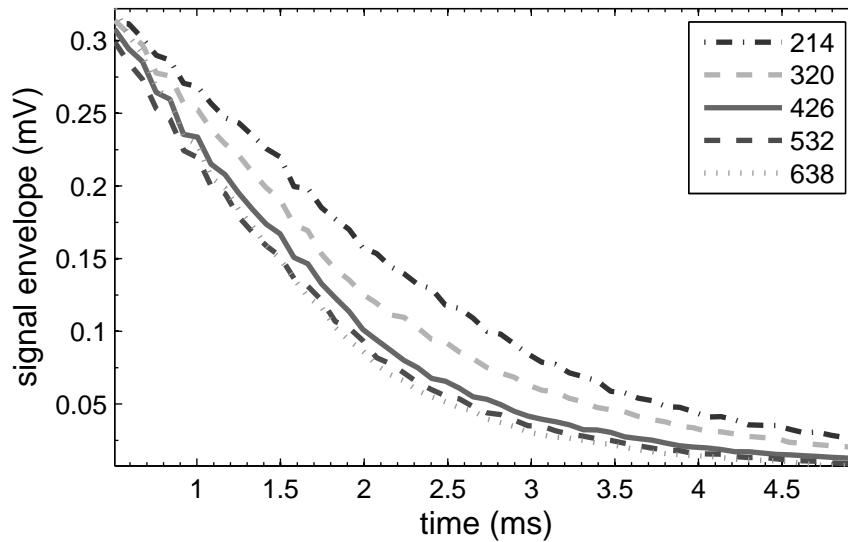

FIG. 3.13 The damping of the signal envelope increases with grid spacing. These envelope signals are for a driven equal number of ^{7}BeH$^+$ and ^{7}Li$^+$ ion plasma at a density of 10^{13} m^{-3} using 10 million simulated particles. The numbers in the legend are in units of grid points.

To understand how the number of simulated particles influences our time signal, we ran our two cases using different number of simulated particles. In the case of ^{7}Be$^+$ and ^{7}Li$^+$, we found that one million simulated particles was sufficient. More simulated particles did not change the plasma dynamics. In the case of ^{7}BeH$^+$ and ^{7}Li$^+$, Fig. 3.14 illustrates how increasing the num-

ber of simulation particles lessens the damping in the time wall signal. Three million simulated particles would have been sufficient, but we chose to use ten million simulated particles to resolve confidently this damping in the wall signal.
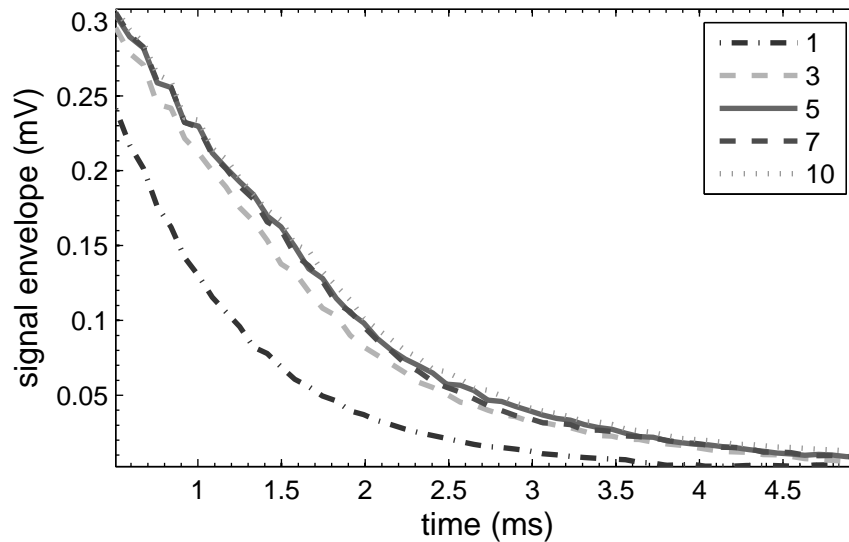

FIG. 3.14 The damping of the signal envelope lessens as the number of millions of simulated particles increases. These envelope signals are for a driven equal number of ^{7}BeH$^+$ and ^{7}Li$^+$ ion plasma at a density of 10^{13} m^{-3} using 426 grid points. The numbers in the legend are in units of millions of simulated particles.

3.10 INITIAL EXPLORATION

In our studies we first began by exploring the driving parameters and the plasma's time response. Given a bandwidth window, we usually knew approximately at what frequency to drive the system. However the time and amplitude were determined by experimentation. We did our best to minimize our drive time to minimize the total computation time. We usually used a drive time which would allow for the desired drive spectrum to be resolved. For our ^{7}Be$^+$ case it was about 100 μs and for the ^{7}BeH$^+$ case, it was 500 μs. We also maintain our drive time and amplitude in a linear plasma's

time response regime. In other words, we reduced drive time or amplitude if we lost particles in our simulation or the time response was nonlinear in nature.

Figures 3.15 and 3.16 illustrate a study of these drive parameters for the case of equal amounts of $^7\text{Be}^+$ and $^7\text{Li}^+$. Figure 3.15 illustrates how changing the drive time with a drive amplitude of 10 mV is nonlinear in the time response. Initially, the response is quadratic for the first 0.1 ms where the ions had the drive applied for only 100 cyclotron cycles. After 0.1 ms it becomes closer to linear, but is still visibly nonlinear. This is possibly from the interaction between the two species. Figure 3.16 illustrates how changing the drive amplitude with a drive time of 0.1 ms is linear in response for many orders of magnitudes as is expected.
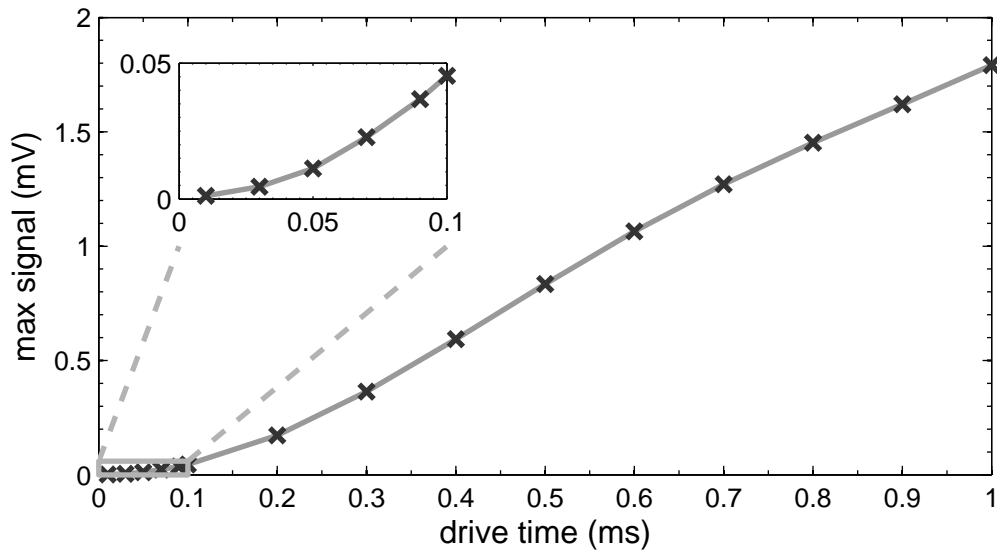
FIG. 3.15 Drive time vs. maximum of time signal with drive amplitude of 10 mV. This signal is for equal numbers of $^7Be^+$ and $^7Li^+$ ions at a density of 10^{13} m^{-3}. Notice how the response is nonlinear.

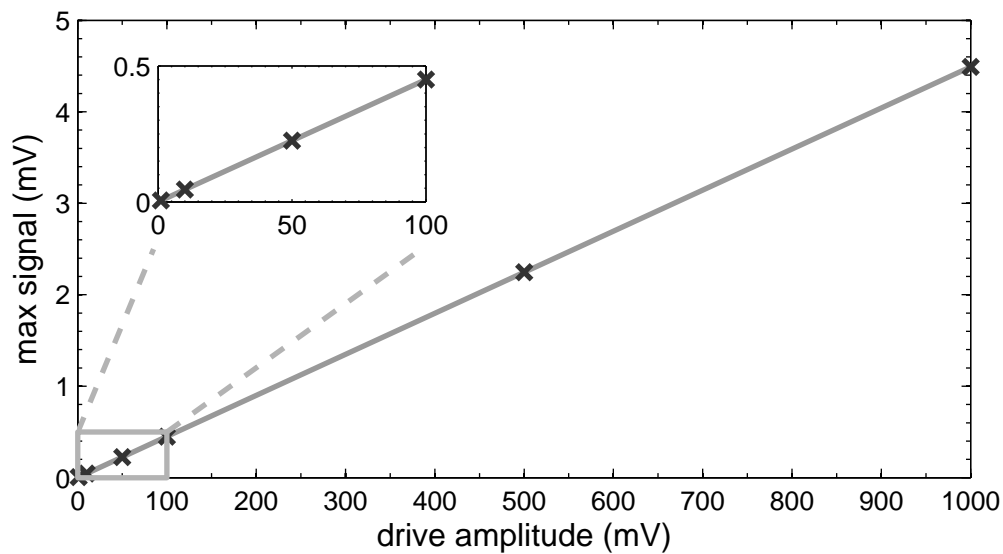**FIG. 3.16** Drive amplitude vs. maximum of time signal with drive time for 100 μs. This signal is for equal numbers of $^7Be^+$ and $^7Li^+$ ions at a density of 10^{13} m^{-3}. The response is linear and the fitted equation is max signal = $(4.491\times10^{-3}$ drive amplitude + $3.794\times10^{-4})$ mV.

CHAPTER 4

RESULTS

4.1 OVERVIEW

Our goal in simulating the FTICR-MS signal of a decaying ^{7}Be ion plasma was to see if we could quantify the abundances of ^{7}Be$^+$ and ^{7}Li$^+$ in our ^{7}Be experiment. In our experiment, we realized that we also needed to study ^{7}BeH$^+$ and ^{7}Li$^+$ which are likely to be found in our vacuum system.[42]

Previously, Mitchell[28] as well as Nikolaev *et. al*[43] have shown in 3D PIC codes that the FTICR-MS spectral peaks of two similarly massed ions coalesce at high ion density. The cyclotron frequency difference between the two masses were about 459 Hz. Their respective spectral peaks coalesced at a total of 350 000 ions in a cubical trap with a one inch side. This was done near the plasma regime. The radius of their ion clouds were on the order of two Debye lengths. In our case and for our simulation, the difference in cyclotron frequency between ^{7}Be$^+$ and ^{7}Li$^+$ is about 124 Hz. Our plasma radius, therefore, is about 50 Debye lengths, more than a order of magnitude larger than in the 3D PIC codes of Mitchell and Nikolaev *et. al*. This means that we are well within the plasma regime. Since we have more Debye lengths per radius, we require a finer computational grid. In particular, we use a grid of 426×426. This compares to Nikolaev's finest grid of 128×128×128. The computational cost of extending to a much finer grid to three dimensions is unacceptably high. Staying in two dimensions also allows us to work with more particles in our simulations, reducing the shot noise in the results. As a result, we are extending these previous simulation studies into the plasma regime where additional effects can possibly exist.

We begin by looking at the overall physical picture of our system illustrated in Fig. 4.1. We are confining a two component ion plasma in a cylindrical trap. In our study, the two components vary in their relative abundances. We detect the induced signal from this plasma on two opposing quarter wall sectors. To obtain our FTICR-MS signal, we take the difference between the two sectors and fast Fourier transform this signal.
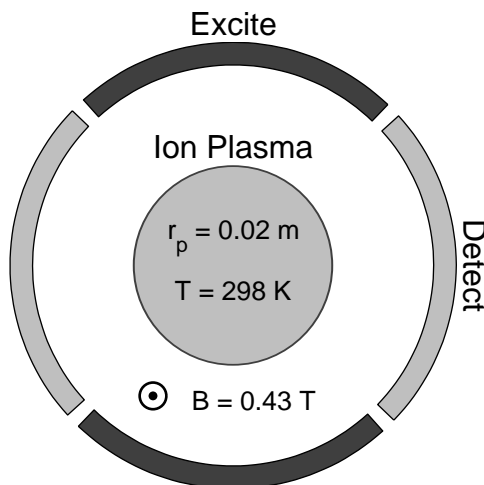
Excite

Ion Plasma

$r_p = 0.02$ m

T = 298 K

⊙ B = 0.43 T

Detect

FIG. 4.1 Physical parameters for our simulation.

As a reference to what "normal" FTICR-MS spectra look like at lower density regime, Fig. 4.2 illustrates how the FTICR-MS spectra for $^7Be^+$ and $^7Li^+$ ions changes with their relative abundances. We observe two separate spectral peaks for $^7Be^+$ and $^7Li^+$ ions. These peaks are at the respective ideal cyclotron frequencies of 941 028 Hz for $^7Be^+$ and 941 152 Hz for $^7Li^+$. The peak's height varies with the abundances of each species. As the abundance of $^7Be^+$ ions decreases, its peak magnitude decreases and the $^7Li^+$ peak magnitude increases.

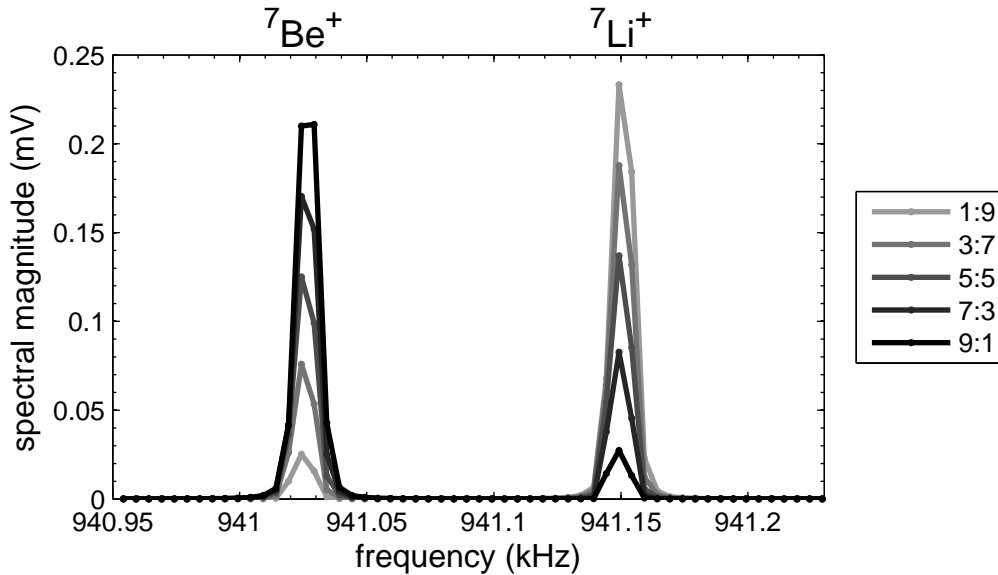**FIG. 4.2** This is a composite figure of the FTICR-MS spectra for $^7Be^+$ and $^7Li^+$ ions at a central density of 10^9 m^{-3} as their relative abundances are varied. The numbers in the legend are the ratios between the two species. 9:1 means 90% $^7Be^+$ and 10% $^7Li^+$.

4.2 $^7BE^+$ AND $^7LI^+$

Coalescence study

We began by looking at the coalescence of the spectral peaks of $^7Be^+$ and $^7Li^+$ as the central densities are varied from 10^9 to 10^{13} m^{-3}. This was done for equal abundances of each species. Figure 4.3 illustrates the changes which occurred in both the time history and spectrum as the central density is increased.

In time, we observe a beating pattern which disappears for central densities exceeding 10^{11} m^{-3}. Note that the strength of the time signal also increases with particle number. In the frequency spectrum, we observe that the two separate peaks for $^7Be^+$ and $^7Li^+$ merge into a single, coalesced peak at about a central density of 10^{11} m^{-3}. This spectral peak also downshifts from the ideal cyclotron frequency as central density increases. This shift becomes significant above 10^{12} m^{-3}.
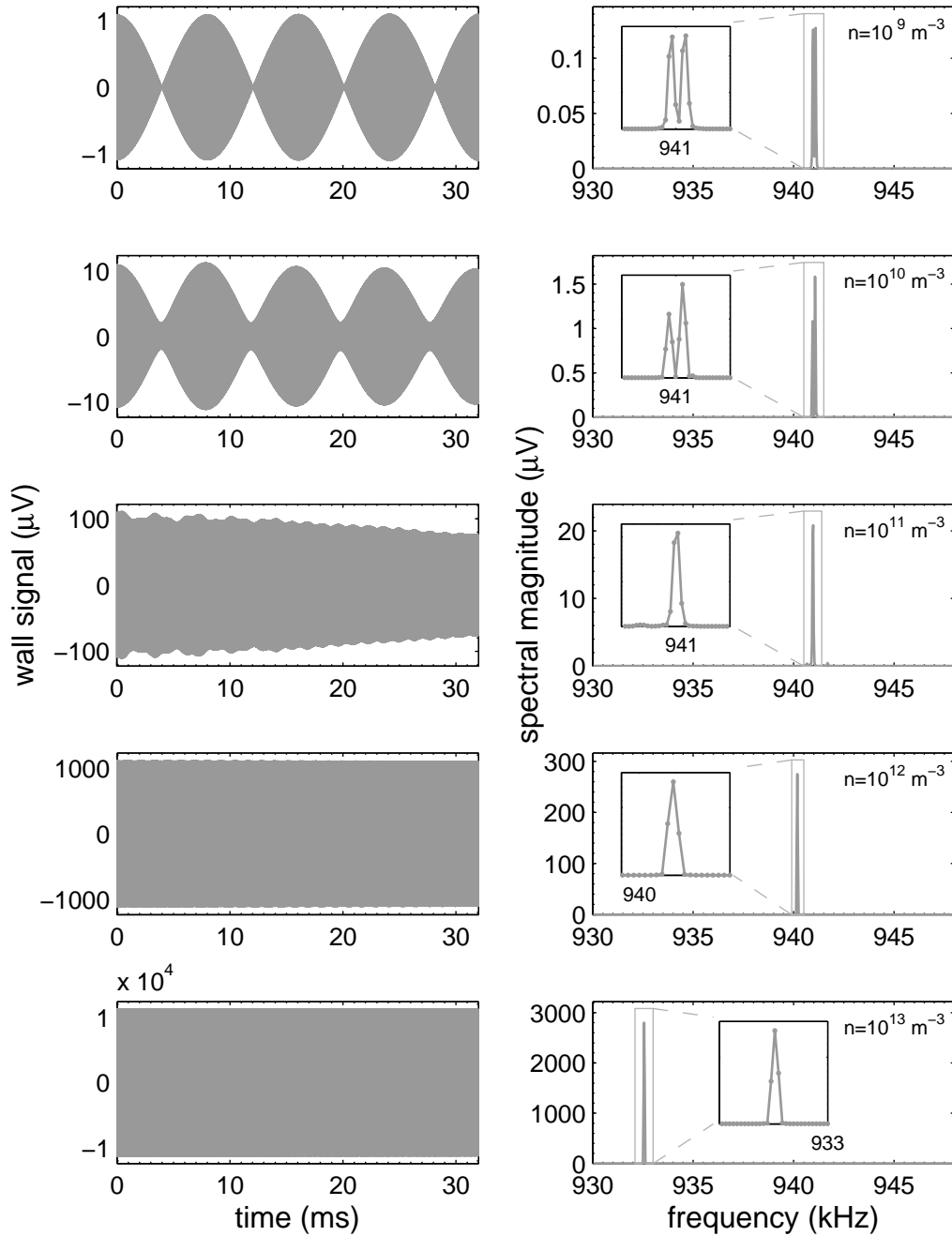
FIG. 4.3 Coalescence of $^7Be^+$ and $^7Li^+$ spectral peaks as density increases. In the time domain, the beating pattern disappears as density increases. In the frequency domain, the two separate peaks merge into one and shifts in frequency. The central density is shown on the top right corner of the frequency domain graph.

Using Mitchell's stability condition[28], we verify that our spectral peaks coalesce at a density of 10^{11} m^{-3}. This condition was originally derived from Peurrung and Kouzes[44]. Mitchell rewrote this condition in term of a ratio of the plasma density to Brillouin density n/n_B as follows:

$$\frac{n}{n_B} > 13 \left(\frac{r_c}{R_p} \right) \left(\frac{\Delta f_c}{f_c} \right) \tag{4.1}$$

where r_c is the cyclotron radius, R_p is the plasma radius, Δf_c is the difference in cyclotron frequency, and f_c is the cyclotron frequency. For this condition, we use 2.6 mm as the cyclotron radius and $^7Be^+$ cyclotron frequency. This cyclotron radius is the average of the two species' excited center of mass radial position. In our simulation this critical condition is $n/n_B > 0.022\%$. At a density of 10^{11} m^{-3}, $n/n_B = 0.14\%$ and the condition is satisfied. As shown in Fig. 4.3, the spectral peaks coalesce at a density 10^{11} m^{-3} while at 10^{10} m^{-3}, $n/n_B = 0.014\%$ and the condition is not satisfied.

Our experiment requires 10^9 ions for decay statistics. This corresponds to a central density of 10^{13} m^{-3}. As a result, the $^7Be^+$ and $^7Li^+$ spectral peaks will have coalesced in our experiment. Nonetheless, we would like to determine if we can quantify the relative abundances in this plasma regime. At this density, the Debye length is 377 μm, which is much less than the 2 cm radius of the plasma.

Quantifying abundances by frequency shift

In order to study quantitatively how this coalesced peak varies with the relative abundances of $^7Be^+$ and $^7Li^+$, we use the parameters in Table 4.1 in our 2D PIC code. The length of our simulations corresponds to 200 ms. This took about two and half weeks to run on a supercomputer to resolve the cyclotron frequency difference of about 124 Hz. With a 200 ms time signal, we have a frequency resolution of 5 Hz.

TABLE 4.1 Simulation parameters for the case of $^7Be^+$ and $^7Li^+$ at a density of 10^{13} m^{-3}.

number of grid points	426
number of simulated particles	10^6
time step	30 ns
drive time	0.1 ms
drive spectral amplitude	2.5 V
drive frequency range	931 kHz to 933 kHz
time observed	200 ms

Figure 4.4 presents some of our results of how the frequency of the coalesced peak changes for different ratios of $^7Be^+$ and $^7Li^+$. Clearly, the merged peak moves from the $^7Be^+$ frequency to the $^7Li^+$ frequency as the ratio of $^7Li^+$ to $^7Be^+$ increases. The spectral magnitude is about the same for each ratio when we apply the same drive to our system.

Figure 4.5 shows that the coalesced peak frequency shifts linearly as a function of the $^7Li^+$ fraction. The coalesced peak is the weighted average of the individual cyclotron frequencies of $^7Be^+$ and $^7Li^+$ downshifted by 8 458 Hz. The diocotron frequency for this case is 8 500 which is a 42 Hz difference from the overall shift. This difference is comparable to the numerical shift in the frequency due to the finite step size as shown in Fig. 3.12. Based on our simulations it is reasonable to say that the individual cyclotron frequencies are downshifted by the diocotron frequency.

This has been discussed previously in Sec. 2.2. Indeed, Mitchell[28] observed a frequency shift for two ion clouds of similar masses and with equal numbers at high density in a 3D PIC code. He attributed this shift to the image charge interaction acting on the phase locked ion cloud. Further, Mitchell and Smith[27] observed that the coalesced peak frequency showed a dependence on the relative abundance. Our results extend these observations into the plasma regime. The individual
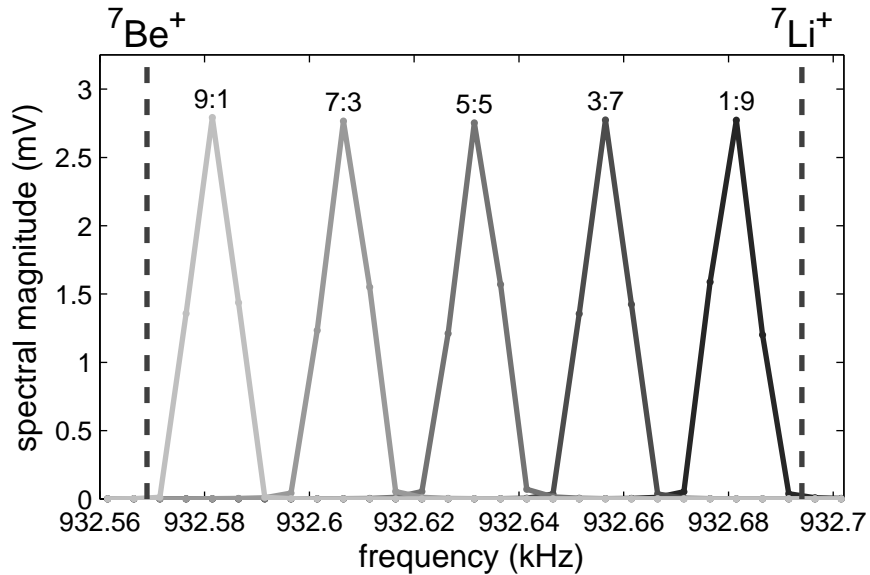
FIG. 4.4 This is a composite figure of the FTICR-MS spectra for $^7Be^+$ and $^7Li^+$ ions at a central density of 10^{13} m^{-3} as their relative abundances are varied. The dashed straight lines represent the peak frequencies for pure $^7Be^+$ or $^7Li^+$ ions. The value on top of each peak is the corresponding ratio of $^7Be^+$ to $^7Li^+$. The spectral peak shifts from left to right as $^7Be^+$ ions become $^7Li^+$ ions.

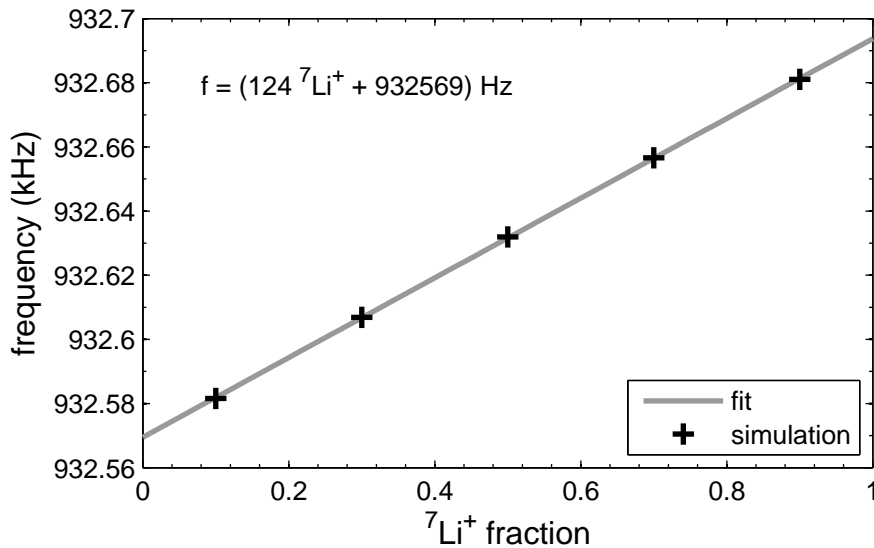**FIG. 4.5** Analysis of how the FTICR-MS merged spectral peak frequency for $^7Be^+$ and $^7Li^+$ ions at a central density of 10^{13} m^{-3} varies with the fraction of $^7Li^+$. The variation is linear in $^7Li^+$ fraction. The fitted equation is written in the top left corner.

cyclotron frequencies are shifted by the diocotron frequency of the plasma. The coalesced peak frequency does depend on the relative abundances of the two species even in the plasma regime.

One limiting factor in this measurement of relative abundances is the frequency difference between the two species. In our case, there is about 124 Hz difference between the cyclotron frequency of the two species. In our simulation, our frequency resolution is at 5 Hz. So, we can only differentiate differences in ratio in 5% increments in the simulation.

Another limiting factor in measuring the relative abundances is the downshifting by the diocotron frequency. By measuring the diocotron frequency at the same accuracy as our coalesced peak, we can determine this overall shift. However, the magnetic field in our experiment is likely to drift somewhat in time. This magnetic field drift will cause our respective frequencies to drift too. It will therefore be imperative to measure both the coalesced peak and the diocotron peak frequencies at each time. The frequency of an impurity species, which we will almost certainly have within our plasma, may possibly provide another reference frequency with which to make our abundance measurement. Such an approach still needs to be investigated in our 2D PIC simulation.

In short, we can determine the abundance of each species by the peak frequency shift from their individual cyclotron frequencies downshifted by the diocotron frequency. As long as we can measure both the coalesced peak frequency and the diocotron frequency, we should be able to determine the abundances of $^7Be^+$ and $^7Li^+$ within our plasma. The study reported here is unique because we have systematically quantified the abundances of two species with a coalesced spectral peak frequency and have extended previous observations into the plasma regime.

4.3 ^{7}BEH$^+$ AND ^{7}LI$^+$

Time signal decays

From talking to Bollinger *et. al*[42] at NIST, a group which has confined Be ion plasma in similar traps to ours, we learned that our ^{7}Be ion plasma will quickly become a ^{7}BeH$^+$ ion plasma. So it was imperative that we also studied the ^{7}BeH$^+$ and ^{7}Li$^+$ case. This case is advantageous compared to ^{7}Be$^+$ and ^{7}Li$^+$ case because the mass difference in this last case is larger. As a result, their individual peaks would not coalesce but be two separate peaks.

However, we noticed that the time signal quickly decays at the density of 10^{13} m^{-3} for equal amounts of ^{7}BeH$^+$ and ^{7}Li$^+$ ions. At other ratios the time signal decays more slowly. Figure 4.6 illustrates this decay effect. To confirm that this was a plasma effect, we studied this signal at a density of 10^9 m^{-3}. At this low density, we observed that the time signal remained at a constant level as in case of the ^{7}Be$^+$ and ^{7}Li$^+$.

Finally, we decided to see if the decay effect decreases with driving amplitude. Figure 4.7 illustrates this decay for equal amounts of ^{7}BeH$^+$ and ^{7}Li$^+$ ions as we decrease our driving spectral amplitude from 33 mV to 0.33 mV. At 33 mV, the decay occurs within less than 0.5 ms. By 3.33 mV, it has slowed down to about 5 ms. At 1 mV, as well as at 0.33 mV, it seems that we get something of a normal exponential decay. The exact detail of why this decay occurs is still not well understood.

In reviewing the literature, we found that this decay phenomenon is similar in nature to the colloquially known "nipple effect" or spontaneous loss of coherence catastrophe (SLCC) spoken of by Nikolaev[43] and Aizikov[45]. This effect probably has to do physically with the energy transfer between the cyclotron frequencies of each species and the $\mathbf{E} \times \mathbf{B}$ drift rotation frequency of this ion plasma. Even with this obstacle, we moved forward to see if we could quantify the abundances of a ^{7}BeH$^+$ and ^{7}Li$^+$ ion plasma.
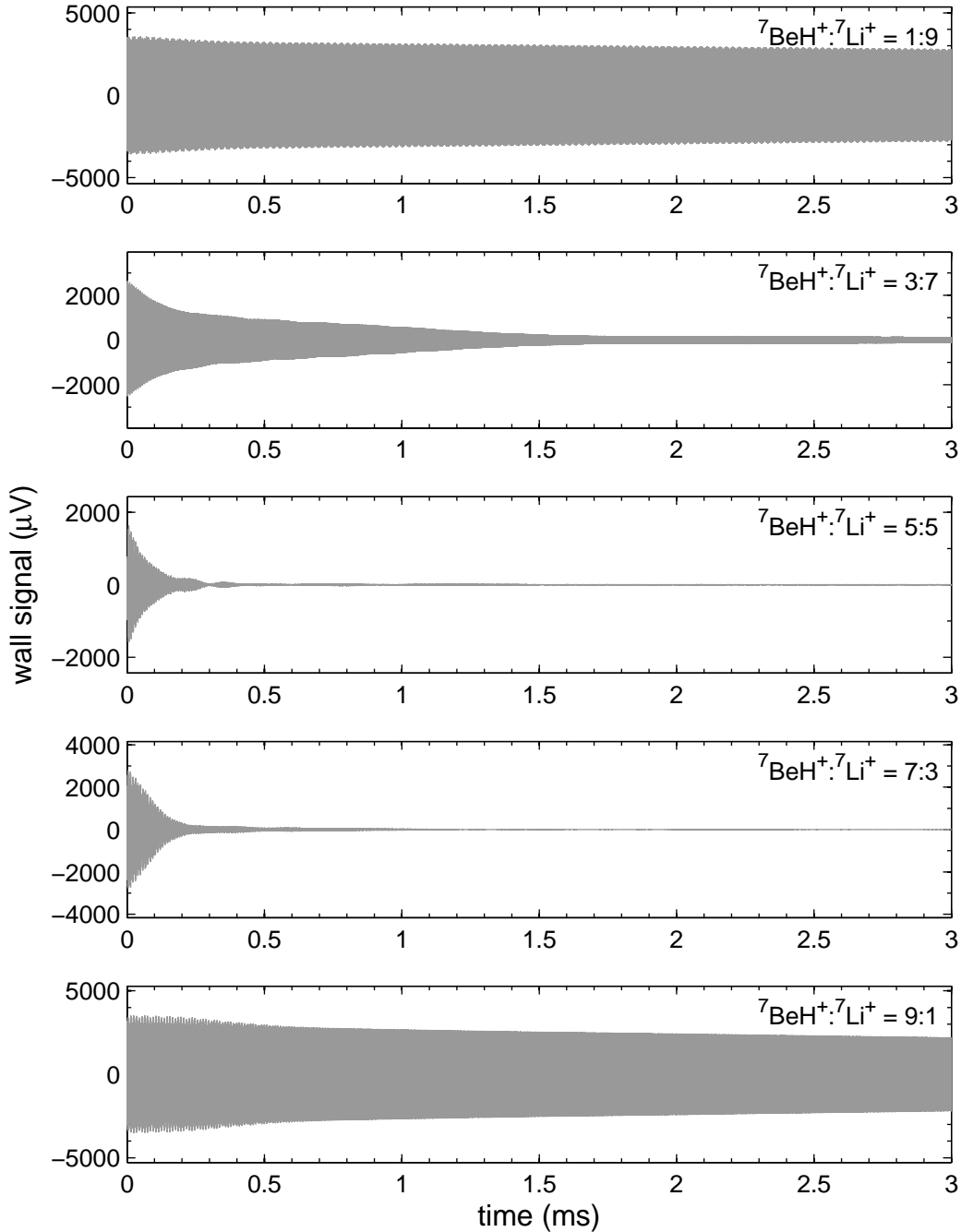
FIG. 4.6 $^7BeH^+$ and $^7Li^+$ ion plasma time signal decay as the fraction of species in the plasma is varied. This is at the density of 10^{13} m^{-3}. This run used a 426×426 grid, a driving spectral amplitude of 33.33 mV, and 10 million simulated particles. Notice how the decay is fastest when there are equal amounts of each species. The fraction of species is labeled on the top right corner.
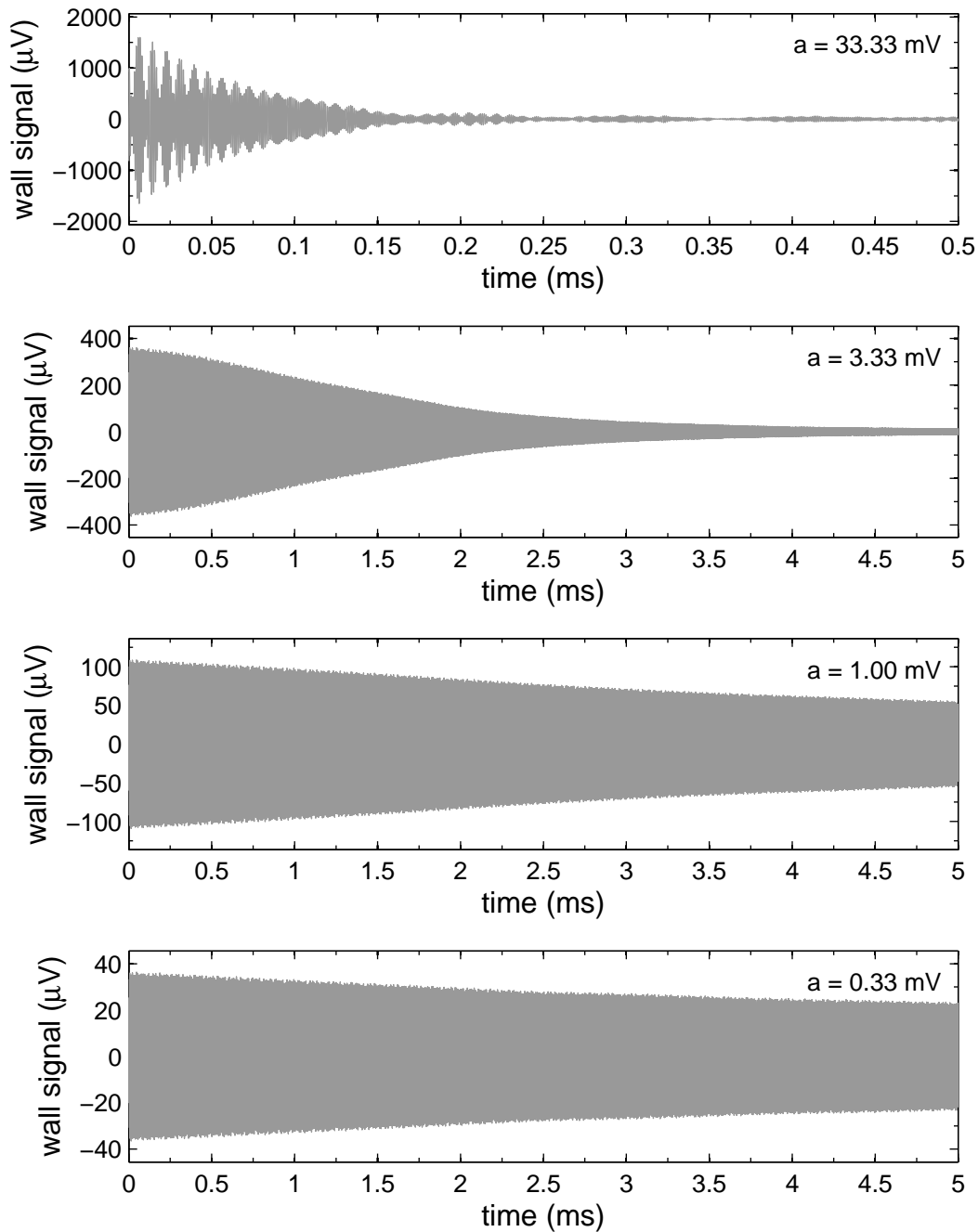
FIG. 4.7 This illustrates how the time signal for equal amounts of $^7BeH^+$ and $^7Li^+$ ions varies as driving spectral amplitude. This is at the density of 10^{13} m^{-3}. This run used a 426×426 grid and 10 million simulation particles. The driving spectral amplitude is labeled on the top right corner.

Quantifying abundances by frequency shift

In order to study quantitatively how the relative abundances of $^7BeH^+$ and $^7Li^+$ are related to their FTICR-MS spectrum, we use the parameters in Table 4.2 in our 2D PIC code. Note that we increase the number of simulated particles to better resolve this decay effect. We have also applied a spectral amplitude of 1 mV to both broadband frequency ranges.

TABLE 4.2   Simulation parameters for $^7BeH^+$ and $^7Li^+$ case at density of 10^{13} m^{-3}.

number of grid points	426
number of simulated particles	10^7
time step	30 ns
drive time	0.5 ms
drive spectral amplitude	1 mV
1st drive frequency range	785 kHz to 815 kHz
2nd drive frequency range	905 kHz to 935 kHz
time observed	5 ms

Figure 4.8 illustrates how the $^7BeH^+$ and $^7Li^+$ spectral peaks remain separate and vary with their abundances. Their respective spectral peak frequencies shift with abundance. As the density of the $^7BeH^+$ ions decrease, the two spectral peaks move farther apart and away from the pure $^7BeH^+$ peak. Meanwhile, the $^7Li^+$ spectral peak moves toward its pure spectral peak. Another interesting aspect we examined is how the spectral peak amplitudes also change with their relative abundances.

To begin, we analyze the relationship of the peak frequency shifts to the relative abundances. Our initial guess was that the peak frequency shifted linearly. However on closer inspection, we found that it was not quite linear. Using the model of two overlapping rods of charge revolving
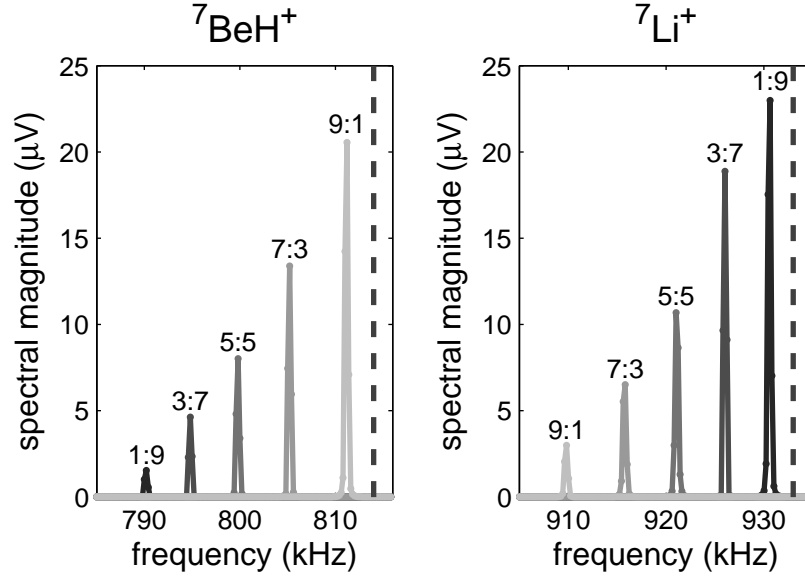
FIG. 4.8 This is a composite figure of the FTICR-MS spectra for $^7BeH^+$ and $^7Li^+$ at a central density of 10^{13} m^{-3} as their relative abundances are varied. The dashed straight line in each frame represents the peak frequency for pure $^7BeH^+$ or $^7Li^+$. The number on top of each peak is the ratio of $^7BeH^+$ to $^7Li^+$. As $^7BeH^+$ decays into $^7Li^+$, the $^7BeH^+$ spectral peak shifts down away from the pure $^7BeH^+$ spectral peak while the $^7Li^+$ peak shifts up toward the pure $^7Li^+$ peak.

around a central axis in a grounded cylinder, as discussed in Sec. 2.4, we are able to model the peak frequency shift. Figure 4.9 compares the results of this analytical model with our simulation results for the peak frequency as a function of $^7Li^+$ fraction. The agreement is very good; the average percent error is 0.005% (about 50 Hz), where we define the average percent error, *APE*,

$$APE = \frac{1}{N} \sum_{i=1}^{N} \frac{|A_i - A_m|}{A_m} \times 100\%. \tag{4.2}$$

N is the number of measurements, A_i is the simulation value, and A_m is the model value.

This analytical model also works for a central number density of $n_0 = 10^{12}$ m^{-3}. In this case, the average percent error is 0.006% (about 60 Hz), which is basically the same error as seen at higher density. In Fig. 4.10, we can see a small discrepancy. The simulation peak frequencies are downshifted from the analytical model. The reason that the discrepancy is more visible in the 10^{12}

m^{-3} case is that the frequency spread increases with density. For 10^{12} m^{-3} the spread is 2 kHz, while for 10^{13} m^{-3} it is about 20 kHz. A possible explanation for this consistent discrepancy is that our model assumes a uniform radial density profile while in our simulation the radial density profile changes with time.

We have also confirmed that our analytical model agrees with the multispecies cold plasma theory used by Sarid, Anderegg, and Driscoll[31] to quantify the cyclotron frequency shifts in a Mg^+ ion plasma. This theory was derived by Davidson[32] using a macroscopic cold fluid description. This theory was discussed in Sec. 2.3. It is not as intuitive as our model, but it does extend to higher order m angular modes and to more than two species. Therefore we have two analytical models which can be used to determine the abundances of $^7BeH^+$ and $^7Li^+$ from their peak frequency shifts.

One limitation in this measurement, of course, is that the decay of the time signal limits the frequency resolution in our FFT. In $^7BeH^+$ and $^7Li^+$ studies, our simulation runs were for 5 ms. This corresponds to a frequency resolution of about 200 Hz. In the 10^{12} m^{-3} measurement, we could have run longer to get better resolution because the decay is slower at this lower density. However, the average percent error between the two densities is only 0.001% (about 10 Hz) which is reasonable to say that they exhibit the same error.

Another limitation is that these two analytical models do not take into account all the effects that exist in our plasma, such as the radial density profile. Both models assume a uniform constant radial profile for the plasma. Our simulated plasma will deviate some from this uniform constant profile. As Sarid, Anderegg, and Driscoll[31] found they could not explain the shifts of the minor species in their Mg^+ ion plasma experiment, so these models will probably not be able to account for all the species we will have experimentally.
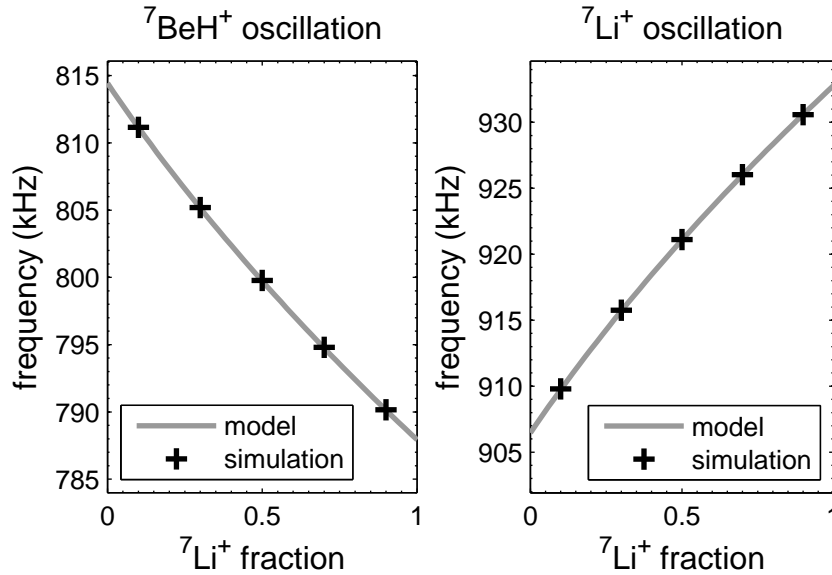
FIG. 4.9 Analysis of how the FTICR-MS spectral peaks for $^7BeH^+$ and $^7Li^+$ vary with fraction of $^7Li^+$ at a central density of 10^{13} m^{-3}. It fits well with an analytical model using two charge columns in a grounded cylinder. The average percent error between the model and simulation is 0.005%.

FIG. 4.10 Analysis of how the FTICR-MS spectral peaks for $^7BeH^+$ and $^7Li^+$ vary with fraction of $^7Li^+$ at a central density of 10^{12} m^{-3}. It fits well with an analytical model using two charge columns in a grounded cylinder. The average percent error between the model and simulation is 0.006%.
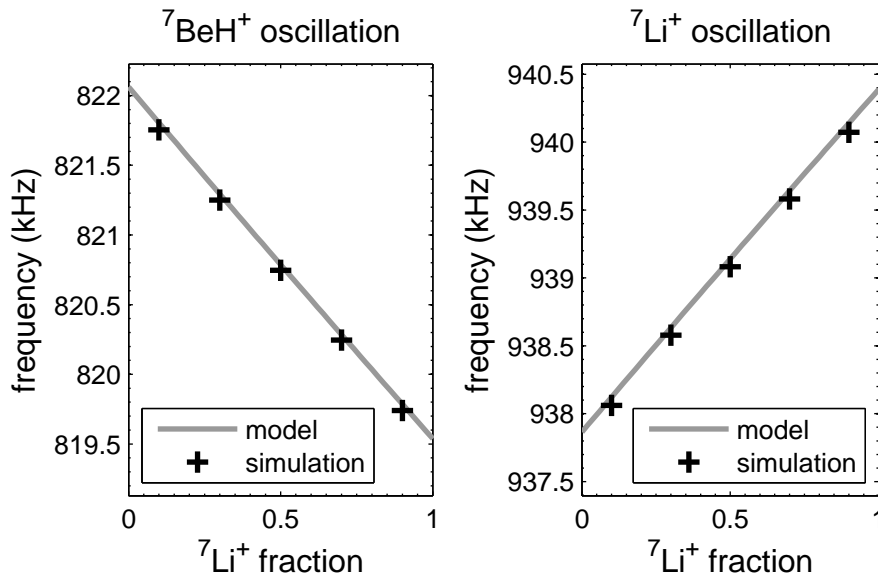
Quantifying abundances by peak heights and areas

We can determine relative abundances by analyzing the peak height and the area under the peak. Figures 4.11 and 4.12 illustrate how these quantities vary with relative abundance. As can be seen from the graphs, the trends are not linear, but by calibrating these trends with the code we can use this as an independent measure of abundances. Also notice that the trend line for the area is smoother than the trend line for the peak height because of the averaging which occurs when taking the area under the spectral peak.

Limitations for measuring abundances with peak height and area are similar to those for measuring frequency shifts. The largest limiting factor is the signal decay rate which determines our frequency resolution. Another is the numerical error from the simulation, which in the case of $^7Be^+$ and $^7Li^+$ could be on the order of 50 Hz for absolute frequency measurements.

In contrast to the $^7Be^+$ and $^7Li^+$ case, our abundance resolution can be greater if we can prevent the signal from decaying too much. A measurement accuracy of 0.005% of 10^9 ions is 50 thousands ions, three orders of magnitude better than for the $^7Be^+$ and $^7Li^+$ peak measurement. We also have two independent measurements of the abundances by using the spectral peak shifts and the changes in height or area. This may be sufficiently advantageous experimentally that we may want to encourage the formation $^7BeH^+$ by adding hydrogen to our trap to bond with the initial $^7Be^+$ ion plasma.

In short, we can determine the abundance of $^7BeH^+$ and $^7Li^+$ by the peak frequency shift by using two analytical models. We can also determine their abundances by calibrating the changes in their spectral peak height and area in our simulation. This abundance measurement by peak height and area is unique to this study and has not been seen in the plasma regime before.
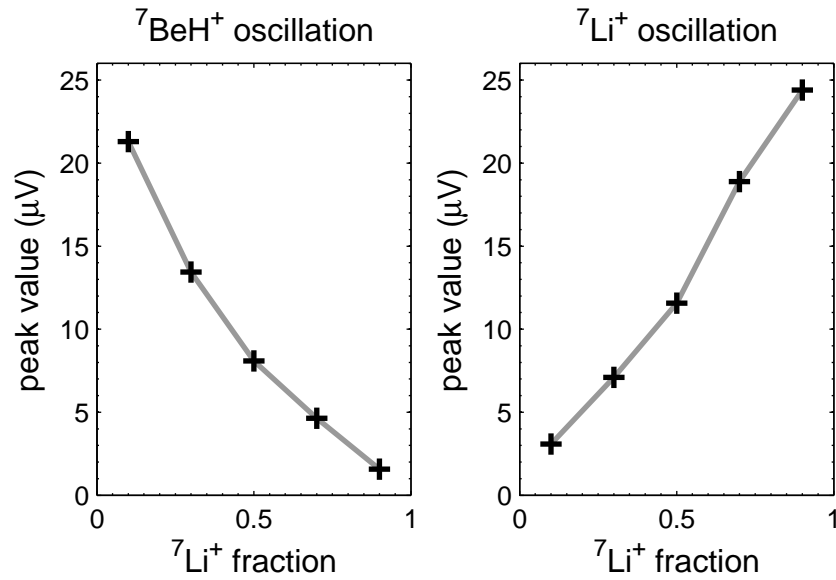
FIG. 4.11 Analysis of how the FTICR-MS spectral peak height for $^7BeH^+$ and $^7Li^+$ varies with fraction of $^7Li^+$ at a central density of 10^{13} m^{-3}.
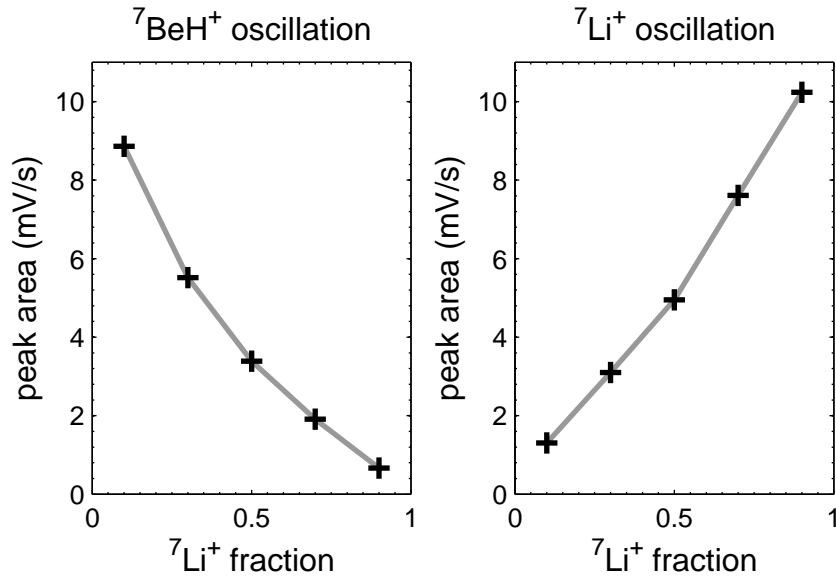

FIG. 4.12 Analysis of how the area under the FTICR-MS spectral peak for $^7BeH^+$ and $^7Li^+$ varies with fraction of $^7Li^+$ at a central density of 10^{13} m^{-3}. We use a trapezoidal method to calculate the area.

4.4 Summary

Our 2D PIC simulation has shown that we can quantify the abundances of ^{7}Be and ^{7}Li in a decaying ^{7}Be ion plasma. This can be done for both ^{7}Be$^+$ to ^{7}Li$^+$ and ^{7}BeH$^+$ to ^{7}Li$^+$ cases even under non-ideal conditions, where collective plasma effects are significant. For ^{7}Be$^+$, the frequency variation is linear with ^{7}Li$^+$ fraction. The frequency variation is not linear for ^{7}BeH$^+$, but we have two analytical models that appear to correctly predict the frequency shifts. In addition, the peak height and area changes in the case of ^{7}BeH$^+$ and ^{7}Li$^+$ provide an independent measure of the abundance. We can calibrate this nonlinear relationship with our simulation. Thus the peak height and area measurement together with the peak frequency shifts will increase our precision and confidence in measuring the abundances of ^{7}BeH$^+$ and ^{7}Li$^+$ in our ^{7}Be experiment. In summary, these two independent measurements of abundance and the increase of accuracy in the ^{7}BeH$^+$ case leads us to encourage the conversion of the initial ^{7}Be$^+$ plasma into ^{7}BeH$^+$ plasma.

We have extend the previous results such as the shift of the coalesced peak frequency into the plasma regime. The multispecies cold fluid theory has also verified our 2D PIC simulation. However, the study reported here is unique in that we have systematically examined how the particular spectra for ^{7}Be$^+$ or ^{7}BeH$^+$ and ^{7}Li$^+$ change with abundances in the plasma regime. The unique question that we have asked is "Can we measure the relative abundances of ^{7}Be$^+$ and ^{7}Li$^+$ species in an ion plasma?" The answer is that yes we can. Another distinctive feature of our study is that we have found that in the plasma regime, we can use the peak height and area to measure the abundances in the case of ^{7}BeH$^+$ and ^{7}Li$^+$.

In distinction to Mitchell[28] and Nikolaev *et. al*[43] 3D PIC codes, our 2D PIC code is able to produce accurate and trustworthy results within the plasma regime. To our knowledge, this has never been done before. The price we have to pay is that the code is 2D. Were our code to be extended to 3D, we would no longer be able to run for as long (up to 0.2 ms) in order to resolve

our cyclotron frequency difference. Indeed, we needed our current grid resolution (426×426) in order to resolve a Debye length of a few hundred microns. In short our 2D code was specifically designed to observe the cyclotron motions of two or more species in the plasma regime.

4.5 RECOMMENDATIONS

For future investigations, I recommend that we further study the physics of the $^7\text{BeH}^+$ and $^7\text{Li}^+$ case using this 2D PIC simulation to understand the decay mechanism so that we may better detect their relative abundances. I also recommend that we study a $^7\text{BeH}^+$, $^7\text{Be}^+$, and $^7\text{Li}^+$ case to see if it will assist in the calibration of $^7\text{Be}^+$ and $^7\text{Li}^+$ abundance measurement. This three species case will also be closer to our real ^7Be experiment case. Lastly, I recommend that we parallelize this code, so that it may run more efficiently.

In conclusion, this simulation has been and is a useful tool to understand our diagnostics in our ^7Be experiment. It has shown that we can detect the relative abundances of $^7\text{Li}^+$ to either $^7\text{BeH}^+$ or $^7\text{Be}^+$.

BIBLIOGRAPHY

[1] D. R. Tilley, C. M. Cheves, J. L. Godwin, G. M. Hale, H. M. Hofmann, J. H. Kelley, C. G. Sheu, and H. R. Weller, "Energy levels of light nuclei A=5, 6, 7," *Nuclear Physics A*, **708**, 3 (2002). 1

[2] National Nuclear Data Center, Brookhaven National Laboratory, "NuDat (Nuclear Structure and Decay Data)," http://www.nndc.bnl.gov/nudat2, (accessed August 13, 2008). 1

[3] R. B. Roberts, N. P. Heydenburg, and G. L. Locher, "Radioactivity of Be^7," *Phys. Rev.*, **53**, 1016 (1938). 1

[4] R. Davis, "Nuclear Recoil Following Neutrino Emission from Beryllium 7," *Phys. Rev.*, **86**, 976 (1952). 1

[5] J. R. Arnold and H. A. Al-Salih, "Beryllium-7 Produced by Cosmic Rays," *Science*, **121**, 451 (1955). 1

[6] J. N. Bahcall, "Electron Capture and Nuclear Matrix Elements of Be^7," *Phys. Rev.*, **128**, 1297 (1962). 1

[7] T. Ohtsuki, H. Yuki, M. Muto, J. Kasagi, and K. Ohno, "Enhanced Electron-Capture Decay Rate of ^7Be Encapsulated in C_{60} Cages," *Phys. Rev. Lett.*, **93**, 112501 (2004). 2

[8] C.-A. Huh, "Dependence of the decay rate of ^7Be on chemical forms," *Earth and Planetary Science Letters*, **171**, 325 (1999). 2

[9] L. gun Liu and C.-A. Huh, "Effect of pressure on the decay rate of ^7Be," *Earth and Planetary Science Letters*, **180**, 163 (2000). 2

[10] E. Segrè and C. E. Wiegand, "Experiments on the Effect of Atomic Electrons on the Decay Constant of Be^7," *Phys. Rev.*, **75**, 39 (1949). 2

[11] M. A. Hutchison, "Computational analysis of the relative decay constants for $^7Be, ^7Be^+$, and $^7Be^{++}$," Senior thesis, Brigham Young University (2009). 2

[12] D. K. Olson, "Development of a MeVVA based beryllium-7 plasma source," M.S. thesis, Brigham Young University (2007). 3

[13] K. M. Giraud, "Simulation and manufacture of a quadrupole mass filter for a ^7Be ion plasma," Senior thesis, Brigham Young University (2008). 3

[14] J. H. Malmberg and J. S. deGrassie, "Properties of Nonneutral Plasma," *Phys. Rev. Lett.*, **35**, 577 (1975). 4

[15] X.-P. Huang, F. Anderegg, E. M. Hollmann, C. F. Driscoll, and T. M. O'Neil, "Steady-State Confinement of Non-neutral Plasmas by Rotating Electric Fields," *Phys. Rev. Lett.*, **78**, 875 (1997). 4

[16] B. Hicks, "Development and characterization of an FT-ICR/MS system for a non-neutral plasma," Senior thesis, Brigham Young University (2008). 5

[17] C. J.Dawson, "Integrator Circuitry used to determine the radial profile of a non-neutral plasma," Senior thesis, Brigham Young University (2008). 5

[18] A. G. Marshall, C. L. Hendrickson, and G. S. Jackson, "Fourier transform ion cyclotron resonance mass spectrometry: A primer," *Mass Spectrom. Rev.*, **17**, 1 (1998). 6

[19] B. Asamoto, editor, *FT-ICR/MS: analytical applications of fourier transform ion cyclotron resonance mass spectrometry* (VCH Publishers, New York, NY, 1991). 6

[20] J. Huang, P. W. Tiedemann, D. P. Land, R. T. McIver, and J. C. Hemminger, "Dynamics of ion coupling in an FTMS ion trap and resulting effects on mass spectra, including isotope ratios," *International Journal of Mass Spectrometry and Ion Processes*, **134**, 11 (1994). 8, 9

[21] Y. Naito and M. Inoue, "Peak Confluence Phenomenon in Fourier Transform Ion Cyclotron Resonance Mass Spectrometry," *Journal of the Mass Spectrometry Society of Japan*, **42**, 1 (1994). 8, 9

[22] J. B. Jeffries, S. E. Barlow, and G. H. Dunn, "Theory of space-charge shift of ion cyclotron resonance frequencies," *International Journal of Mass Spectrometry and Ion Processes*, **54**, 169 (1983). 9

[23] M. V. Gorshkov, A. G. Marshall, and E. N. Nikolaev, "Analysis and elimination of systematic errors originating from Coulomb mutual interaction and image charge in fourier transform ion cyclotron resonance precise mass difference measurements," *Journal of the American Society for Mass Spectrometry*, **4**, 855 (1993). 9, 12

[24] A. J. Peurrung and R. T. Kouzes, "Analysis of space-charge effects in cyclotron resonance mass spectrometry as coupled gyrator phenomena," *International Journal of Mass Spectrometry and Ion Processes*, **145**, 139 (1995). 9

[25] Y. Naito and M. Inoue, "Collective motion of ions in an ion trap for Fourier transform ion cyclotron resonance mass spectrometry," *International Journal of Mass Spectrometry and Ion Processes*, **157-158**, 85 (1996). 9

[26] D. W. Mitchell and R. D. Smith, "Cyclotron motion of two Coulombically interacting ion clouds with implications to Fourier-transform ion cyclotron resonance mass spectrometry," *Phys. Rev. E*, **52**, 4366 (1995). 9

[27] D. W. Mitchell and R. D. Smith, "Prediction of a Space Charge Induced Upper Molecular Mass Limit Towards Achieving Unit Mass Resolution in Fourier Transform Ion Cyclotron Resonance Mass Spectrometry," *Journal of Mass Spectrometry*, **31**, 771 (1996). 9, 49

[28] D. W. Mitchell, "Realistic simulation of the ion cyclotron resonance mass spectrometer using a distributed three-dimensional particle-in-cell code," *J. Am. Soc. Mass Spectrom.*, **10**, 136 (1999). 9, 44, 48, 49, 61

[29] I. A. Boldin and E. N. Nikolaev, "Theory of peak coalescence in Fourier transform ion cyclotron resonance mass spectrometry," *Rapid Communications in Mass Spectrometry*, **23**, 3213 (2009). 9

[30] R. W. Gould and M. A. LaPointe, "Cyclotron resonance phenomena in a pure electron plasma," *Physics of Fluids B: Plasma Physics*, **4**, 2038 (1992). 10

[31] E. Sarid, F. Anderegg, and C. F. Driscoll, "Cyclotron resonance phenomena in a non-neutral multispecies ion plasma," *Phys. Plasmas*, **2**, 2895 (1995). 10, 11, 57

[32] R. C. Davidson, *Physics of Nonneutral Plasma* (Addison-Wesley, Redwood City, CA, 1990), p. 258. 10, 57

[33] J. P. Boris, "Relativistic Plasma Simulation – Optimization of a Hybrid Code," in J. P. Boris and R. A. Shanny, editors, "Proceedings of the Fourth Conference on the Numerical Simulation of Plasmas," (Naval Research Laboratory, Washington, D. C., 2–3 November 1970), pp. 3–67. 19

[34] O. Buneman, "Inversion of the Helmholtz (or Laplace-Poisson) operator for slab geometry," *Journal of Computational Physics*, **12**, 124 (1973). 19

[35] C. K. Birdsall and A. B. Langdon, *Plasma Physics via Computer Simulation* (McGraw-Hill, New York, NY, 1985). 20, 29

[36] A. G. Marshall, T. C. L. Wang, and T. L. Ricca, "Tailored excitation for Fourier transform ion cyclotron mass spectrometry," *Journal of the American Chemical Society*, **107**, 7893 (1985). 24

[37] L. Chen, T. C. L. Wang, T. L. Ricca, and A. G. Marshall, "Phase-modulated stored waveform inverse Fourier transform excitation for trapped ion mass spectrometry," *Analytical Chemistry*, **59**, 449 (1987). 24

[38] S. Guan and J. Robert T. McIver, "Optimal phase modulation in stored wave form inverse Fourier transform excitation for Fourier transform mass spectrometry. I. Basic algorithm," *The Journal of Chemical Physics*, **92**, 5841 (1990). 24

[39] R. W. Hockney and J. W. Eastwood, *Computer Simulation Using Particles* (Taylor & Francis, New York, NY, 1988). 29

[40] K. L. Goodner, K. E. Milgram, K. R. Williams, C. H. Watson, and J. R. Eyler, "Quantitation of ion abundances in fourier transform ion cyclotron resonance mass spectrometry," *Journal of the American Society for Mass Spectrometry*, **9**, 1204 (1998). 35

[41] C. D. Keefe and M. B. Comisarow, "A Family of Highly Accurate Interpolation Functions for Magnitude-Mode Fourier Transform Spectroscopy," *Applied Spectroscopy*, **44**, 600 (1990). 37

[42] M. J. Jensen, T. Hasegawa, J. J. Bollinger, and D. H. E. Dubin, "Rapid Heating of a Strongly Coupled Plasma near the Solid-Liquid Phase Transition," *Physical Review Letters*, **94**, 025001 (2005). 44, 52

[43] E. N. Nikolaev, R. M. A. Heeren, A. M. Popov, A. V. Pozdneev, and K. S. Chingin, "Realistic modeling of ion cloud motion in a Fourier transform ion cyclotron resonance cell by use of a particle-in-cell approach," *Rapid Communications in Mass Spectrometry*, **21**, 3527 (2007). 44, 52, 61

[44] A. J. Peurrung and R. T. Kouzes, "Long-term coherence of the cyclotron mode in a trapped ion cloud," *Phys. Rev. E*, **49**, 4362 (1994). 48

[45] K. Aizikov, R. Mathur, and P. B. O'Connor, "The Spontaneous Loss of Coherence Catastrophe in Fourier Transform Ion Cyclotron Resonance Mass Spectrometry," *Journal of the American Society for Mass Spectrometry*, **20**, 247 (2009). 52